

THESIS FOR THE DEGREE OF LICENTIATE OF ENGINEERING

Phased-Array-Fed Reflector Antenna Systems for Radio Astronomy and Earth Observations

OLEG IUPIKOV



CHALMERS

Department of Signals and Systems
CHALMERS UNIVERSITY OF TECHNOLOGY

Göteborg, Sweden 2014

Phased-Array-Fed Reflector Antenna Systems for Radio Astronomy and Earth Observations

OLEG IUPIKOV

© OLEG IUPIKOV, 2014.

Technical report number: R014/2014

ISSN 1403-266X

Department of Signals and Systems

Division of Antenna Systems

CHALMERS UNIVERSITY OF TECHNOLOGY

SE-412 96 Göteborg

Sweden

Telephone: +46 (0)31 – 772 1000

Email: oleg.iupikov@chalmers.se

Typeset by the author using L^AT_EX.

Chalmers Reproservice
Göteborg, Sweden 2014

To my family

“Look deep into nature, and then you will understand everything better”
-Albert Einstein

Abstract

Dense Phased Array Feeds (PAFs) for reflector antennas have numerous advantages over traditional cluster feeds of horns in a one-horn-per-beam configuration, especially in RF-imaging applications which require multiple simultaneously formed and closely overlapped beams. However, the accurate analysis and design of such PAF systems represents a challenging problem, both from an EM-modeling and beamforming optimization point of view. The current work addresses some of these challenges and consists of two main parts.

In the first part the mutual interaction effects that exist between a PAF consisting of many densely packed antenna elements and an electrically large reflector antenna are investigated. For that purpose the iterative CBFM-PO method has been developed. This method not only allows one to tackle this problem in a time-efficient and accurate manner, but also provides physical insight into the feed-reflector coupling mechanism and allows to quantify its effect on the antenna impedance and radiation characteristics. Numerous numerical examples of large reflector antennas with various representative feeds (e.g. a single dipole feed and complex PAFs of hundreds of elements) are also presented and some of them are validated experimentally.

The second part of the thesis is devoted to the optimization of PAF beamformers and covers two application examples: (i) microwave satellite radiometers for accurate ocean surveillance; and (ii) radio telescopes for wide field-of-view sky surveys. Based on the initial requirements for future antenna systems, which are currently being formulated for these applications, we propose various figures-of-merit and describe the corresponding optimal beamforming algorithms that have been developed. Studies into these numerical examples demonstrate how optimal beamforming strategies can help to greatly improve the antenna system characteristics (e.g. beam efficiency, side-lobe level and sensitivity in the presence of the noise) as well as to reduce the complexity of the beam calibration models and overall phased array feed design.

Keywords: phased array feeds, reflector antenna feeds, beamforming, feed-reflector interaction, radio telescopes, satellite radiometers.

Preface

This thesis is in partial fulfillment for the degree of Licentiate of Engineering at Chalmers University of Technology.

The work that has resulted in this thesis was carried out between December 2011 and October 2014 and has been performed within the Division of Antenna Systems at the Department of Signals and Systems, Chalmers. Associate Professor Marianna Ivashina has been both the examiner and main supervisor, and Assistant Professor Rob Maaskant has been the co-supervisor.

The work has been supported by a project grant “System Modelering och Optimering av Gruppantennor för Digital Lobformning” from the Swedish Research Council (VR) and a grant “Study on Advanced Multiple-Beam Radiometers” (contract 4000107369-12-NL-MH) from the European Space Agency (ESA).

Acknowledgments

First and foremost, I wish to thank my supervisor Associate Professor Marianna Ivashina for the opportunity to work on challenging and relevant research topics, and for her continuous guidance and encouragement during these years. I would also like to thank my co-supervisor Assistant Professor Rob Maaskant for numerous fruitful discussions related to my work, and for the infinite support in such complicated topics as numerical methods for electromagnetic modeling, electromagnetic theory, and so on. I would like to express my appreciation to Professor Per-Simon Kildal for creating a great and friendly research environment in the Antenna Systems Division. Also, thanks to all of you I have met my beloved Esperanza :)

Thanks to my colleagues at the Onsala Space Observatory, especially to Prof. John Conway and Dr. Miroslav Panteleev, for providing me with interesting department service tasks related to the Square Kilometer Array (SKA) project, which was also beneficial for my PhD project as I could improve large parts of Matlab code.

I would also like to thank Kees van 't Klooster from ESA, Knud Pontoppidan, Per Heighwood Nielsen and Cecilia Cappellin from TICRA for the interesting and fruitful collaboration on new satellite radiometers, and Andre Young from Stellenbosch University for common work on calibration techniques for radio telescopes.

I would like to acknowledge Wim van Cappellen from ASTRON, The Netherlands, for providing us with measurements of the Vivaldi antenna PAF (APERTIF), that were made at the Westerbork Synthesis Radio Telescope.

My special thanks go to all the former and current colleagues of the Signals and Systems Department for creating a nice and enjoyable working environment: Aidin, Hasan, Ahmed, Elena, Carlo, Chen, Astrid, and Ashraf. We've had a lot of fun and enjoyable moments both at work and afterwork time.

And of course, my most sincere gratitude to my parents and my family – Esperanza and Marc – for granting me a new sense of life and accompanying me in this scientific journey.

Oleg

List of Publications

This thesis is based on the work contained in the following appended papers:

Paper 1

O. Iupikov, R. Maaskant, and M. Ivashina, “Towards the Understanding of the Interaction Effects Between Reflector Antennas and Phased Array Feeds”, in *Proceedings of the International Conference on Electromagnetics in Advanced Applications, ICEAA 2012*, Cape Town, South Africa, September 2012, pp. 792–795.

Paper 2

O. Iupikov, R. Maaskant, and M. Ivashina, “A plane wave approximation in the computation of multiscattering effects in reflector systems”, in *Proceedings of the 7th European Conference on Antennas and Propagation, EUCAP 2013*, Gothenburg, Sweden, April 2013, pp. 3828–3832.

Paper 3

O. Iupikov, R. Maaskant, M. Ivashina, A. Young, and P.S. Kildal, “Fast and Accurate Analysis of Reflector Antennas with Phased Array Feeds including Multiple Reflections between Feed and Reflector”, *IEEE Transactions on Antennas and Propagation*, vol.62, no.7, 2014, pp. 3450–3462.

Paper 4

C. Cappellin, K. Pontoppidan, P. H. Nielsen, N. Skou, S. S. Søbjerg, M. Ivashina, O. Iupikov, A. Ihle, D. Hartmann, and K. v. 't Klooster, “Novel Multi-Beam Radiometers for Accurate Ocean Surveillance”, in *Proceedings of the 8th European Conference on Antennas and Propagation, EUCAP 2014*, The Hague, The Netherlands, April 2014, pp. 1–5

Paper 5

O. Iupikov, M. Ivashina, K. Pontoppidan, P. H. Nielsen, C. Cappellin, N. Skou, S. S. Søbjerg, , A. Ihle, D. Hartmann, and K. v. 't Klooster, “Dense Focal Plane Arrays for Pushbroom Satellite Radiometers”, in *Proceedings of the 8th European Conference on Antennas and Propagation, EUCAP 2014*, The Hague, The Netherlands, April 2014, pp. 1–5

LIST OF PUBLICATIONS

Paper 6

A. Young; M.V. Ivashina; R. Maaskant; O.A. Iupikov; D.B. Davidson, “Improving the Calibration Efficiency of an Array Fed Reflector Antenna Through Constrained Beamforming”, *IEEE Transactions on Antennas and Propagation*, vol.61, no.7, July 2013, pp. 3538–3545.

Contents

Abstract	i
Preface	iii
Acknowledgments	v
List of Publications	vii
Contents	ix

I Introductory Chapters

1 Introduction	1
1.1 Next generation radio telescopes	1
1.2 Satellite radiometers for Earth observations	3
1.3 Modeling, design and calibration challenges of novel Phased Array Feeds	4
1.4 Goal and outline of the thesis	6
2 Electromagnetic Analysis of Reflector Antennas with Phased Array Feeds Including Feed-Reflector Multiple Reflection Effects	9
2.1 Analysis method: formulation and validation of the iterative CBFM-PO approach	9
2.2 Acceleration techniques	10
2.2.1 Single plane wave approximation of the reflector field	12
2.2.2 Plane wave spectrum (PWS) approach	15
2.2.3 Near-field interpolation (NFI) technique	18
2.2.4 Analysis of PWE and NFI errors and simulation times	20
2.3 Experimental verification of the CBFM-PO approach with acceleration techniques	21
2.4 Numerical studies for different types of reflector antenna feeds	21
2.5 Conclusions	24

3	Phased Array Feed Beamforming Strategies for Earth Observations and Radio Astronomy	27
3.1	Application 1: Satellite radiometers for accurate ocean surveillance	27
3.1.1	Performance requirements	27
3.1.2	Reflector antenna and PAF designs methodology	30
3.1.3	Optimization procedure for the PAF beamformers	32
3.1.4	Numerical results: Optimized PAF+beamformer design	37
3.2	Application 2: Radio telescopes for wide field-of-view sky surveys	43
3.3	Conclusions	44
4	Conclusions and future work	47
	References	49

II Included Papers

Paper 1	Towards the Understanding of the Interaction Effects Between Reflector Antennas and Phased Array Feeds	61
1	Introduction	61
2	Analysis methodology	62
3	Numerical Results	63
4	Conclusions	67
	References	67
Paper 2	A Plane Wave Approximation In The Computation Of Multiscattering Effects In Reflector Systems	71
1	Introduction	71
2	Modeling procedure and numerical results	72
3	Conclusions	76
	References	78
Paper 3	Fast and Accurate Analysis of Reflector Antennas with Phased Array Feeds including Multiple Reflections between Feed and Reflector	83
1	Introduction	83
2	Iterative CBFM-PO Formulation	85
3	Acceleration of the Field Computations	90
3.1	Plane Wave Spectrum Expansion – FFT	91
3.2	Near-Field Interpolation	92
4	Numerical Results	93
4.1	Validation of the Iterative Approach	95

CONTENTS

4.2	Field Approximation Errors	98
4.3	Feed-Reflector Antenna System Performance Study	101
5	Conclusions	106
	References	107
Paper 4 Novel Multi-Beam Radiometers for Accurate Ocean Surveillance		115
1	Introduction	115
2	Optical Design	117
2.1	Conical scanning radiometer antenna	117
2.2	Torus push-brom radiometer antenna	117
3	Antenna Requirements	119
3.1	Acceptable cross-polarization	119
3.2	Acceptable side lobes and distance to coast	119
4	Feed Array Design	119
4.1	Conical scanning radiometer antenna	119
4.2	Torus push-brom radiometer antenna	121
5	Conclusions	125
	References	125
Paper 5 Dense Focal Plane Arrays for Pushbroom Satellite Radiometers		129
1	Introduction	129
2	Antenna Requirements	131
3	FPA-system design	132
3.1	Antenna array model	132
3.2	Beamforming algorithms	133
3.3	Parametric study	133
4	Conclusions	138
5	Acknowledgment	138
	References	138
Paper 6 Improving the Calibration Efficiency of an Array Fed Reflector Antenna Through Constrained Beamforming		143
1	Introduction	143
2	Antenna Pattern Model	145
3	Beamforming Strategy	146
3.1	Number of Constraints and Pattern Calibration Measurements	147
3.2	Constraint Positions	147
3.3	Constraints Vector	148
4	Numerical Results	149
4.1	Beam Directivity and Side Lobe Levels	150

CONTENTS

4.2	Calibration Performance	151
4.3	Comparison of MaxDir and LCMV beamformers	152
5	Conclusions and Recommendations	153
	References	153

Part I

Introductory Chapters

Chapter 1

Introduction

Since recently, several types of so-called “dense” Phased-Array Feed (PAF) systems for reflector antennas have been designed for applications in future instruments for radio astronomy, Earth surface and space observations [1–11]. The main advantage of these PAFs over conventional single-horn feeds and cluster feeds of horns is that the inter-element separation distance of such “dense” PAFs can be much smaller than one wavelength to allows the formation of multiple closely overlapping beams with high efficiency [12]. Another advantage is that these PAFs can be equipped with digital beamformers providing an individual complex excitation per array antenna element and hence can realize an optimal illumination of the reflector aperture [13–18]. These advantageous properties are of great importance both for radio astronomy and Earth observation applications requiring fast and wide field-of-view (FOV) surveys.

1.1 Next generation radio telescopes

The effectiveness of performing wide-field surveys is characterized by the telescope’s survey speed, i.e., the speed at which a certain volume of space can be observed with a given sensitivity. The survey speed is proportional to the size of the instantaneous FOV and the frequency bandwidth, weighted by the sensitivity squared [19]. Present-day aperture synthesis radio telescopes have a limited observation capability due to the fact that only a small part of the sky can be observed simultaneously, which therefore results in a low survey speed. In contrast, using PAFs as a reflector antenna feed allows (i) to increase the receiving sensitivity of the reflector antenna due to better illumination of the dish, and (ii) to form multiple simultaneous beams, which can be closely overlapped, as a result of overlapping sub-arrays forming these beams, to provide a continuous FOV [20].

The FOV of conventional telescopes with single-beam feeds is limited to one half-power beamwidth, where the sensitivity takes the maximum value along the beam axis and gradually decreases from its center. To image a larger region of the sky,

astronomers use the “mosaicing” technique [21]. With this technique, a telescope performs many observations by mechanically steering (scanning) the dish such that the main lobes of the beams generated in subsequent observations closely overlap and form an almost continuous beam envelope when superimposed. The large-field image is therefore formed by composing a mosaic of smaller sized overlapping images taken during these observations. According to Nyquist’s field-sampling theorem, a uniform sensitivity of the combined image is achieved when the beam separation is equal to or smaller than one half of the half-power beamwidth [22]. A larger spacing between the observations results in a sensitivity ripple over the FOV. The maximum allowable ripple will depend on the particular science case.

PAFs can provide many closely overlapping beams in one snapshot, thereby greatly improving the size of the FOV. However, to meet the required field-sampling limit with a cost-effective number of PAF beams, their shapes should be optimized and the maximum achievable sensitivity should be traded against the maximum tolerable sensitivity ripple over the FOV.

In addition to a continuous FOV and high sensitivity, high polarization discrimination is required for large-field surveys [23–25]. For this purpose, the incident field is sampled by two orthogonally polarized receptors or beams. In radio astronomy, the polarization purity of the resulting images is established after extensive offline calibration of the data. In this respect, two antenna design aspects are of particular importance: the stability (i.e. variation over time) of the co- and cross-polarized beams; and the orthogonality of the two beams in the direction of incidence. This requires that the beams are formed simultaneously and span a 2-D basis along which the incident field is decomposed. Future PAF-equipped telescopes are potentially accurate polarimeters thanks to the flexibility that digital beamforming offers. However, although the orthogonality of the beam pair in the direction of observation may be improved electronically, it is important that the intrinsic polarization characteristics of the beams are sufficiently good to minimize such corrections as they may compromise the receiving sensitivity.

Another important concern about radio telescopes is their calibration procedure. This requires accurate models of the instrumental parameters and propagation conditions, which vary over time, so that the model parameters have to be determined during the observation time through a number of calibration measurements [26]. To perform calibration of radio telescopes efficiently, the number of model parameters should be minimal. One of the instrumental parameters that needs accurate characterization is the radiation pattern of the antenna, which is especially challenging for future array based multiple beam radio telescopes due to complexity of such instruments and increased size of the FOV.

To be able to characterize all beams inside the FOV by means of a simple beam model, beamforming techniques can be used to create similarly shaped beams [27, 28]. However, this leads to a loss in the receiving sensitivity requiring us to employ more

advanced but still simple beam models. An attempt to develop such beam model in conjunction with constrained beamforming technique is made in this work.

1.2 Satellite radiometers for Earth observations

Besides radio astronomy applications, PAFs are used in other applications, such as remote sensing of the atmosphere and the Earth’s surface [29,30]. However, there are some important differences in requirements for the instruments in these applications. For example, receivers for Earth remote sensing are typically designed to measure high brightness temperatures (75–300 K) along with short integration times, while in radio astronomy very low brightness temperatures are of interest and the integration time can reach many hours. Therefore, the receiving sensitivity is one of the key instrument characteristics, in particular for radio astronomy applications. On the other hand, for Earth remote sensing applications, such as the assessment of ocean parameters (salinity, sea surface temperature, ocean vector wind), additional specifications for high beam efficiency and measurement accuracy near a coast line are required [10,31].

Recent advances in phased array antenna technologies and low-cost active electronic components open up new possibilities for designing Earth observation instruments, in particular those used for radiometric measurements. Nowadays, two design concepts of microwave radiometers are in use: “push-broom” and “whisk-broom” scanners [32]. Push-broom scanners have an important advantage over whisk-broom scanners in providing larger FOV with higher sensitivity, owing to the fact that these systems can observe a particular area of the ocean for a longer period of time with multiple simultaneous beams. However, the drawback of pushbroom designs – based on conventional focal plane arrays of horns in one-horn-per-beam configuration [33] or clusters with simplistic beamforming schemes [34] – is the FOV varying sensitivity. This variation occurs due to the differences between scanned beams, as these are formed by different horns or clusters, and their large beam separation distance on the oceanic surface, which caused by a large separation distance between the horns.

This drawback may be significantly reduced by employing dense PAFs, i.e., phased-array feeds consisting of many electrically small antenna elements utilizing advanced beamforming schemes [15–17]. This technology has been extensively studied during the last decade in the radio astronomy community, and several telescopes are currently being equipped with dense PAFs [7, 35, 36]. While those systems aim at providing scan ranges of about 5 – 10 beamwidths, for applications as herein considered, the desired scan range (swath range of the radiometer) is one order of magnitude larger [10]. To achieve this large scan-range performance, more complex reflector optics and FPA designs are required. For push-broom radiometers, various optics concepts have been investigated [33], and the optimum solution has been found to be an offset toroidal single reflector antenna, such as illustrated in Fig. 1.1. This reflector structure is rotationally symmetric around its vertical axis, and thus is able

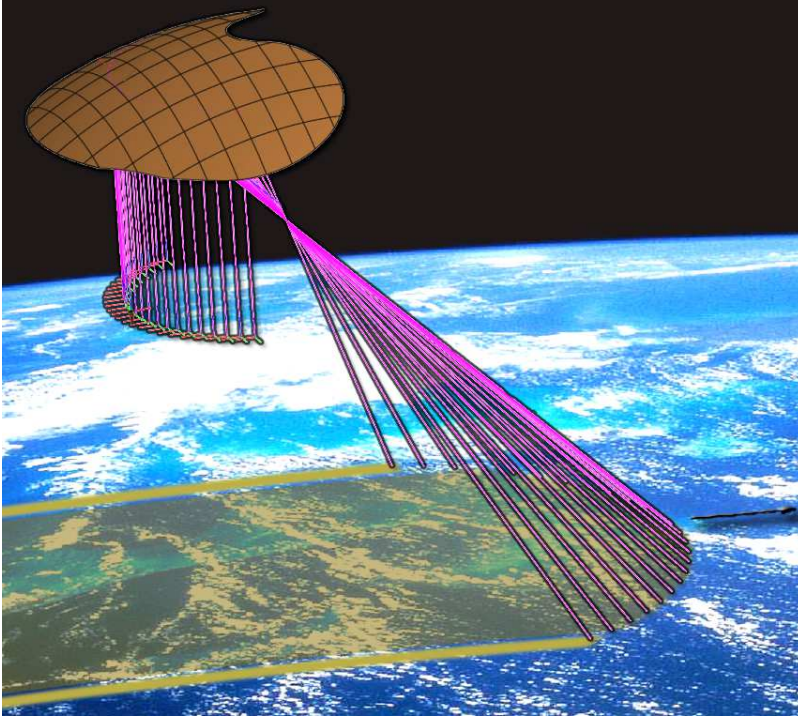


Figure 1.1: Operational principle of a push-broom microwave radiometer, which includes an off-set toroidal reflector antenna fed with a multi-beam focal plane array of horns arranged perpendicular to the flight direction of the spacecraft. Different areas of the ocean-surface are scanned as the spacecraft flies forward.

to cover a wide swath range. However, its aperture field exhibits significant phase errors due to the non-ideal (parabolic) surface of the reflector, which requires the use of a more complex feed system.

1.3 Modeling, design and calibration challenges of novel Phased Array Feeds

The design of the above-mentioned highly complex PAF systems requires the development of accurate and efficient modeling techniques. This is a challenging task considering the size of the reflector used in radio astronomy and Earth observation applications, which can be hundreds of wavelengths in diameter, as well as the size of the PAF, which is too small to be analyzed with an infinite array simulation approach (which also has limitations on the excitation schemes), but too large for the direct usage of full-wave methods implementing plain MoM or FDTD techniques that run on standard computing platforms.

During the last decades, a number of analytical and numerical techniques have been developed to model feed-reflector interaction effects. For example, in [37], the

multiscattered field between the feed and reflector is approximated by a geometric series of on-axis plane wave (PW) fields, each of which is scattered by the antenna feed due to its incident PW at each iteration, and where the amplitudes of these PWs are known in closed-form for a given reflector geometry. This method is very fast and insightful, while MoM-level accuracy can be achieved for single-horn feeds, but not for array feeds as demonstrated in Paper 2. An alternative approach is to use more versatile, though more time-consuming, hybrid numerical methods combining Physical Optics or Gaussian beams for the analysis of reflectors with MoM and/or Mode Matching techniques for horn feeds [38, 39]. The recent article [40] has introduced a PO/Generalized-Scattering-Matrix approach for solving multiple domain problems, and has shown its application to a cluster of disjoint horns. This approach is generic and accurate, but may require the filling of a large scattering matrix for electrically large PAFs and/or multifrequency front-ends (MFFE) that often includes a large extended metal structure [41]. Other hybrid methods, which are not specific for solving the present type of problems, make use of field transformations, field operators, multilevel fast multipole approaches (MLFMA), and matrix modifications [42–45]. Recently, a Krylov subspace iterative method has been combined with an MBF-PO approach for solving feed-reflector problems [46], and complementary to this, an iteration-free CBFM-PO approach has been presented by Hay, where a modified reduced MoM matrix for the array feed is constructed by directly accounting for the presence of the reflector [47]. However, most of these methods are either complicated or slow, or do not allow for the extraction of the feed-reflector interaction effect in a systematic manner.

Besides the efficiency and simplicity of modeling techniques, their accuracy is of great importance too. For example, the present-day radio telescopes with single-beam feeds can achieve a dynamic range upward to $10^6 : 1$ along the on-axis beam direction. However, the off-axis dynamic range is severely limited by uncertainties and temporal instabilities in the beam patterns caused by mispointing and mechanical deformations of the dishes, as well as station-to-station differences in the beam patterns [48, 49]. A number of calibration techniques for dealing with these effects have been proposed and used in practical systems [21, 26]. For novel PAF-based telescopes, the beam calibration is a new challenging field and there is not yet a clear consensus on what constitutes a “good” beam pattern. Furthermore, the mutual coupling between the PAF and the dish(es) of a reflector antenna give rise to a frequency dependent ripple in the antenna radiation and impedance characteristics [50], which exacerbate the calibration, and accurate system models can help alleviating that.

In conclusion, the challenges in modeling, designing and calibrating novel PAFs, are:

- complexity to accurately model a large antenna array of complex antennas, including mutual coupling between array elements;

- cumbersomeness of analyzing a combined PAF-reflector structure due to large size of the reflector and mutual coupling between feed and dish(es) (multi-scale problem);
- development of optimal beamforming algorithms that provide performance requirements on multiple antenna characteristics (e.g. beam efficiency, side-lobe level, sensitivity, etc), while realizing easy-to-calibrate beam shapes and maintaining minimum complexity of the array design (minimum number of elements, similarity of sub-arrays, etc).

1.4 Goal and outline of the thesis

The herein presented work is devoted to address the following challenges: (i) the development of the reflector antenna model, which accounts for the feed-reflector coupling and provides physical insight in the coupling processes, and the analysis of several reflector antennas for different types of feeds and determining which of these feeds are preferred in terms of low feed-reflector coupling and overall antenna performance; (ii) the design of PAFs for an offset toroidal reflector antenna and the development of optimal beamforming algorithms for accurate radiometric measurements; (iii) improving the calibratability of the beam shape of a radio telescope.

This thesis is organized as follows. In **Chapter 2** a general CBFM-PO model of a reflector antenna system is developed. This model is based upon the Jacobi method for solving a system of linear equations iteratively. The Characteristic Basis Function Method (CBFM) is used to model the feed, while the Physical Optics (PO) approach is used to model the current on the reflector at each iteration.

To speed-up the method, several acceleration techniques are developed: the field scattered from the reflector is expanded in a Plane Wave Spectrum (PWS), while the field radiated/scattered by the feed is computed at few near-field points only and then interpolated in order to find the PO current distribution on the reflector surface. This allows us to simulate a reflector antenna 5 – 100 times faster than a pure CBFM-PO approach.

Afterwards, the developed method is used to model large reflector antennas (38λ and 118λ) fed by different types of feeds: (i) a single dipole above a ground plane; (ii) a 20-elements dipole array; (iii) a 121-element dipole array; (iv) a 121-element Vivaldi array; (v) a classical pyramidal horn with aperture size of $\sim 1\lambda$, and; (vi) the same horn with extended ground plane, which could represent a feed cabin of the reflector antenna.

Chapter 3 describes a PAF design procedure and several beamforming strategies. The first part of the chapter is devoted to the application of PAFs in satellite radiometers observing the sea surface, where the requirements for such radiometers are specified and translated to performance figures in terms of antenna character-

1.4. GOAL AND OUTLINE OF THE THESIS

istics. Next, the design procedure of the reflector and the array feed is presented. Afterwards, a customized beamforming algorithm is developed for improving the antenna system characteristics while reducing the size/complexity of the PAF. Finally, numerical results for the designed radiometer equipped with a PAF are presented.

At the end of the chapter it is shown how a constrained beamforming strategy can be used to improve the calibration efficiency of the PAF beam shape of a radio telescope.

The conclusions and recommendations are described in **Chapter 4**.

Chapter 2

Electromagnetic Analysis of Reflector Antennas with Phased Array Feeds Including Feed-Reflector Multiple Reflection Effects

The characterization of feeds in unblocked reflectors and on-axis beams can be handled by the traditional spillover, illumination, polarization and phase subefficiency factors defined for rotationally symmetric reflectors in [51], and be extended to include excitation-dependent decoupling efficiencies of PAFs [20, 52]. The current work investigates the effects of aperture blockage and multiple reflections on the system performance in a more generic fashion than it was done in [37] and [53] for rotationally symmetric antennas and single-pixel feeds.

2.1 Analysis method: formulation and validation of the iterative CBFM-PO approach

The herein proposed analysis method is based on the Jacobi method intended to solve a system of linear equations in an iterative manner. Suppose that the MoM matrix equation for the entire reflector antenna (including both the dish and the feed) is given by

$$\mathbf{Z}\mathbf{I} = \mathbf{V}, \quad (2.1)$$

where \mathbf{Z} is the MoM matrix of size $K \times K$ and \mathbf{V} is a $K \times 1$ excitation vector.

This matrix can be decomposed into matrix blocks as

$$\begin{bmatrix} \mathbf{Z}^{\text{rr}} & \mathbf{Z}^{\text{rf}} \\ \mathbf{Z}^{\text{fr}} & \mathbf{Z}^{\text{ff}} \end{bmatrix} \begin{bmatrix} \mathbf{I}^{\text{r}} \\ \mathbf{I}^{\text{f}} \end{bmatrix} = \begin{bmatrix} \mathbf{V}^{\text{r}} \\ \mathbf{V}^{\text{f}} \end{bmatrix}, \quad (2.2)$$

where \mathbf{Z}^{rr} and \mathbf{Z}^{ff} are the MoM matrix self-blocks of the reflector and feed, respectively¹, and \mathbf{V}^{r} and \mathbf{V}^{f} are the corresponding excitation vectors. The matrix $\mathbf{Z}^{\text{rf}} = (\mathbf{Z}^{\text{fr}})^T$ contains the mutual reactions involving the basis functions on the feed and reflector. The unknown current expansion coefficient vectors are denoted by \mathbf{I}^{r} and \mathbf{I}^{f} .

It can be shown that the solution to Eq. (2.2) can be written as an infinite geometric series (see Paper 3 for the derivation), which, in turn, can be represented by the recursive scheme:

Reflector		Feed	
$\mathbf{I}^{\text{r}} = \sum_{n=0}^{\infty} \mathbf{I}_n^{\text{r}}$	(2.3a)	$\mathbf{I}^{\text{f}} = \sum_{n=0}^{\infty} \mathbf{I}_n^{\text{f}}$	(2.4a)
$\mathbf{I}_{n+1}^{\text{r}} = -(\mathbf{Z}^{\text{rr}})^{-1} \mathbf{Z}^{\text{rf}} \mathbf{I}_n^{\text{f}}$	(2.3b)	$\mathbf{I}_{n+1}^{\text{f}} = -(\mathbf{Z}^{\text{ff}})^{-1} \mathbf{Z}^{\text{fr}} \mathbf{I}_n^{\text{r}}$	(2.4b)
$\mathbf{I}_0^{\text{r}} = (\mathbf{Z}^{\text{rr}})^{-1} \mathbf{V}^{\text{r}}$	(2.3c)	$\mathbf{I}_0^{\text{f}} = (\mathbf{Z}^{\text{ff}})^{-1} \mathbf{V}^{\text{f}}$	(2.4c)

The cross-coupled recursive scheme as formulated by Eqs. (2.3) and (2.4) is exemplified in Fig. 2.1 as a five-step procedure, in which the problem is first solved in isolation to obtain \mathbf{I}_0^{r} and \mathbf{I}_0^{f} . Afterwards, the feed current \mathbf{I}_0^{f} is used to induce the reflector current \mathbf{I}_1^{r} , which is then added up to the initial reflector current. Likewise, the initial reflector current \mathbf{I}_0^{r} is used to induce the feed current \mathbf{I}_1^{f} , which is then added to the initial feed current, and so forth.

Rather than computing the reflector and feed currents through the large-size MoM matrix blocks \mathbf{Z}^{rr} , \mathbf{Z}^{rf} , \mathbf{Z}^{fr} , and \mathbf{Z}^{ff} , additional computational and memory efficient techniques can be used for the rapid computation of these currents at each iteration. Here, the Physical Optics (PO) current is used on the reflector surface and the Characteristic Basis Function Method (CBFM, [55]) is invoked as a MoM enhancement technique for computing the current on the feed. Please see the Paper 3 for details on *how* this is done.

The above described approach has been validated using the MoM solver as part of the CAESAR software [55, 56] and the commercial software FEKO [57] (*c.f.* Paper 3 for details).

2.2 Acceleration techniques

The above-described approach allows us to simulate reflector antennas employing electrically large reflectors fed by complex feeds like PAFs of hundreds of Vivaldi antennas. However, the approach requires the field to be computed at numerous points on both the feed and the reflector surfaces, thereby rendering the field computations

¹Here \mathbf{Z}^{ff} includes the effect of the antenna port terminations [54].

2.2. ACCELERATION TECHNIQUES

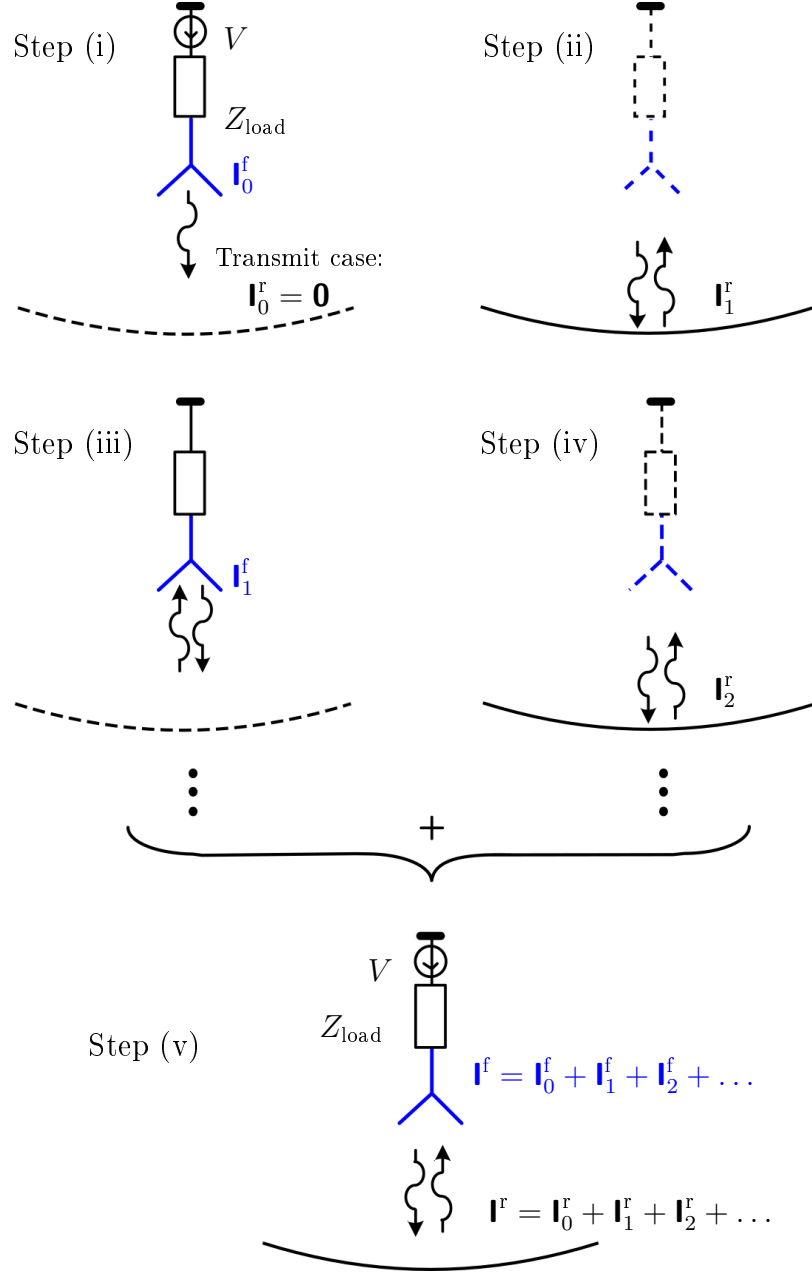


Figure 2.1: Illustration of the cross-coupled iterative scheme for the multiscattering analysis of the feed-reflector interaction effects, as formulated by Eqs. (2.3) and (2.4): (i) The antenna feed radiates in the absence of reflector; (ii) the radiated field from feed scatters from the reflector; (iii) the scattered reflector field is incident on the terminated feed and re-scatters; (iv) the re-scattered field from the feed is incident on the reflector; etc. (v) the final solution for the current is the sum of the induced currents.

inefficient, in particular for complex-shaped electrically large feed antennas employing hundreds of thousands of low-level basis functions. Similarly, one has to cope with a computational burden when calculating the PO equivalent current on elec-

trically large reflectors. In this section a few enhancement techniques are presented that accelerate the field computations while maintaining high accuracy.

2.2.1 Single plane wave approximation of the reflector field

The method described here relies on the fact that the field scattered from the reflector resembles a plane wave (PW), and therefore can be defined by a single PW mode amplitude. In [37] this amplitude is expressed analytically at each iteration for a given reflector geometry, and the scattered field of the feed is approximated by a geometric series of fields scattered by the antenna feed due to an incident plane wave with known amplitude. With reference to Fig. 2.2, the total radiation pattern of the feed \mathbf{E}_{tot} (including feed-reflector coupling) can be expressed as

$$\mathbf{E}_{\text{tot}}(\theta, \phi, r) = \mathbf{E}_r(\theta, \phi, r) + \frac{-\frac{1}{r_0}A(0)\exp(-jk2r_0)}{1 + \frac{1}{r_0}A_s(0)\exp(-jk2r_0)}\mathbf{E}_s(\theta, \phi, r), \quad (2.5)$$

where \mathbf{E}_r and \mathbf{E}_s are the radiation and scattering far-field patterns of the feed in isolation correspondingly, and $A(0)$ and $A_s(0)$ are values of the co-polarization component of these fields in the on-axis direction [see Fig. 2.2(a) and 2.2(b)]; r_0 is the distance between the reflector apex and the phase reference point with respect to which \mathbf{E}_r and \mathbf{E}_s are defined.

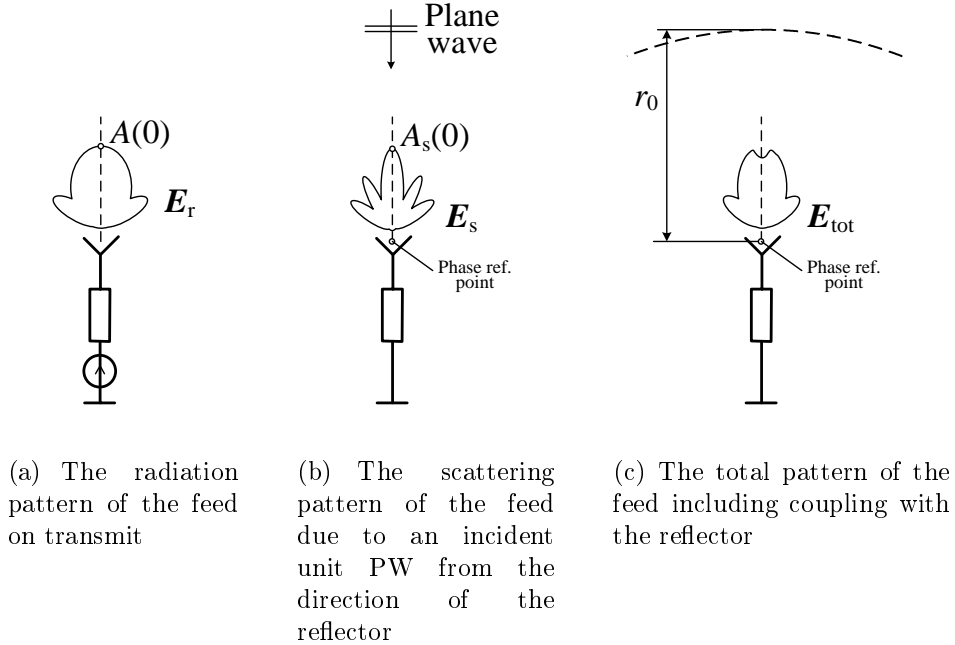


Figure 2.2: Semi-analytical PW approximation as described in [37].

However, as shown in Paper 2, this semi-analytical approach works well only when the feed is small w.r.t. the reflector and when it has low-scattering properties. If the

2.2. ACCELERATION TECHNIQUES

feed becomes electrically large and high-scattering (such as for conventional multi-frequency front-ends in radio telescopes), the accuracy of this method deteriorates. In order to improve the accuracy, the plane wave coefficient can be computed numerically at each iteration. To do so, the field scattered from the reflector is sampled in the focal plane, and the PW coefficient is computed as an average of the sampled field values on a regular grid (see Paper 2 for the derivation):

$$\alpha \approx \frac{1}{K} \sum_{k=1}^K E_p^{\text{ref}}(\mathbf{r}_k), \quad (2.6)$$

where E_p^{ref} is the dominant p -component of the focal field, and the set $\{\mathbf{r}_k\}_{k=1}^K$ are K sample points, which are assumed to be located on a uniform grid in the focal plane.

In summary, the plane-wave-enhanced MoM/PO method consists of the following steps: (i) the antenna feed currents are computed through a method-of-moments (MoM) approach by exciting the antenna port(s) in the absence of the reflector; (ii) these currents generate an EM field which induces PO-currents on the reflector surface; (iii) the PO currents create a scattered field that is tested at only a few points in the focal plane; (iv) the field intensity at the sample points is averaged in accordance with (2.6), and the obtained value is used as the expansion coefficient for the plane wave traveling from the reflector towards the feed; (v) this incident plane wave induces a new current distribution on the feed structure. The steps (ii)–(v) are repeated until a convergence condition is met.

The following three types of feeds are used to illuminate a reflector antenna: (i) a pyramidal horn with aperture diameter in the order of one wavelength; (ii) a pyramidal horn with extended ground plane, and; (iii) an 121-element dual-polarized dipole array (see Fig. 2.3). All antennas are impedance power-matched, so that the antenna component [58] of their corresponding radar cross-section (RCS) is minimized. However, the residual component of the RCS of the horn with ground plane is still high due to the extended metal structure surrounding it, so that this feed is a high scattering antenna and strong feed-reflector coupling can be expected.

The above feeds are used to illuminate two parabolic reflectors with aperture diameters 38λ and 118λ , and the errors introduced by the PW approximation in the focal field and scalars antenna characteristics are computed as

$$\epsilon_1 = \frac{\sqrt{\sum_k |E_{p;k}^{\text{ref}} - E_{p;k}^{\text{mod}}|^2}}{\sqrt{\sum_k |E_{p;k}^{\text{ref}}|^2}} \times 100\% \quad (2.7)$$

$$\epsilon_2 = \frac{|f^{\text{ref}} - f^{\text{mod}}|}{|f^{\text{ref}}|} \times 100\%, \quad (2.8)$$

where $E_{p;k}^{\text{ref}}$ and $E_{p;k}^{\text{mod}}$ are the k -th sample of the discretized p -components of the actual focal E-field $\mathbf{E}^{\text{ref}}(x, y)$ and the focal field modeled by a plane wave $\mathbf{E}^{\text{mod}}(x, y)$ respectively; f^{ref} and f^{mod} is the gain or antenna input impedance, reference and modeled values, respectively. The MoM/PO results without the plane wave approximation are used as the reference solution.

Table 2.1: Errors due to the plane wave approximation

	Focal field		Gain (on-axis)		Gain (@-3 dB)		Impedance	
Reflector diameter D	38λ	118λ	38λ	118λ	38λ	118λ	38λ	118λ

Feed: Pyramidal horn

Parameter variation, %	3.91	1.23	1.98	0.62	3.99	2.16	15.05	4.66
Method:	Error, %							
Method 1	0.3	0.05	0.28	0.05	0.36	0.14	1.37	0.18
Method 2	0.1	0.04	0.16	0.04	0.3	0.13	0.09	0.03

Feed: Pyramidal horn with extended ground plane

Parameter variation, %	139.3	39.1	19.2	3.4	29.4	3.56	43.4	6.1
Method:	Error, %							
Method 1	37.7	1.29	12.7	0.1	10.1	0.17	18.5	0.2
Method 2	11.9	0.48	2.23	0.07	4.71	0.15	12.46	0.11

Feed: 121-element dual-polarized dipole array

Parameter variation, %	8.45	3.28	1.84	0.28	3.68	0.73	5.8	1.7
Method:	Error, %							
Method 1	0.61	0.11	0.21	0.03	0.15	0.02	0.34	0.08
Method 2	0.44	0.1	0.12	0.03	0.08	0.03	0.58	0.05

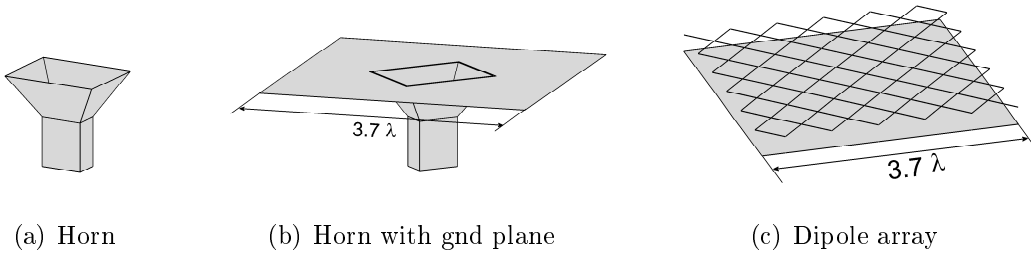


Figure 2.3: Considered feed geometries (in addition to the dipole feed with PEC ground plane): (a) a classical pyramidal horn with aperture length $\sim 1\lambda$; (b) the same horn but with extended ground plane ($\sim 3.7\lambda$), where the ground plane may model the presence of a large feed cabin; (c) an antenna array consisting of 121 0.45λ -dipoles above a ground plane of the same size; (d) the same array, but with the dipoles replaced by wideband tapered slot Vivaldi antennas.

2.2. ACCELERATION TECHNIQUES

The above errors that have been computed for both the semi-analytical and the numerical PW-approximation approaches are summarized in Table 2.1. We will refer to the semi-analytical method as “Method 1”, while the herein proposed approach is denoted as “Method 2”.

The total simulation time (10 frequency points) for the 38λ reflector fed by the considered feeds is shown in Table 2.2.

Table 2.2: Total simulation time

	Horn	Horn with gnd plane	Dipole array	Vivaldi array
MoM-PO, no approximations	9 min 05 sec (100%)	59 min 21 sec (100%)	71 min 09 sec (100%)	197 min 04 sec (100%)
Method 1	0 min 39 sec (7%)	1 min 12 sec (2%)	4 min 49 sec (7%)	33 min 58 sec (17%)
Method 2	2 min 32 sec (28%)	13 min 28 sec (23%)	19 min 19 sec (27%)	67 min 06 sec (34%)

By analyzing Table 2.1 and Table 2.2 the following observations can be made:

- Method 1 is numerically efficient and accurate for small feeds (whose sizes are in the order of one wavelength) and for low-scattering feeds, but fails in case of large high-scattering feeds, such as MFFEs, because the focal field produced by the feed scattering pattern has a high level and a highly tapered shape;
- Method 2 provides a better prediction of all the system parameters, since it accounts for the actual shape of the scattering pattern when fitting the plane wave to it; however, it is slower than Method 1;
- Both methods are accurate in case of large reflectors, because the multiscattering effects are less pronounced (see “Parameter variation” in Table 2.1), and the field scattered from the reflector is close to a plane wave at all iterations.

For the focal field distribution plots and more detailed discussions, see Paper 2.

2.2.2 Plane wave spectrum (PWS) approach

Further improvement of the accuracy can be achieved by expanding the sampled focal field into a plane wave spectrum (PWS) [59–61].

With reference to Fig. 2.4, a grid of sampling points in the xy -plane P in front of the feed at $z = 0$ is chosen for the expansion of the PO radiated field in terms of a PWS. Each PW propagates to a specific observation point \mathbf{r} on the feed where the field \mathbf{E}^{if} is tested. This process of field expansion and PW propagation is realized

through the application of the truncated Fourier Transform pair [59]

$$\mathbf{A}(k_x, k_y) = \frac{1}{2\pi} \int_{-y_{\max}-x_{\max}}^{y_{\max}} \int_{-x_{\max}}^{x_{\max}} \mathbf{E}^{\text{i,f}}(x, y, z=0) e^{j(k_x x + k_y y)} dx dy \quad (2.9a)$$

$$\mathbf{E}^{\text{i,f}}(\mathbf{r}) = \frac{1}{2\pi} \int_{-k_x^{\max}}^{k_x^{\max}} \int_{-k_y^{\max}}^{k_y^{\max}} \mathbf{A}(k_x, k_y) e^{-jk_z z} e^{-j(k_x x + k_y y)} dk_x dk_y \quad (2.9b)$$

where

$$k_z = \begin{cases} \sqrt{k^2 - k_x^2 - k_y^2} & \text{if } k^2 > k_x^2 - k_y^2 \\ -j\sqrt{k_x^2 - k_y^2 - k^2} & \text{otherwise.} \end{cases}, \quad (2.10)$$

and where the spectrum of PWs is limited to only those that are incident on the feed from directions within an angle subtended by the reflector and seen from the center of the plane P (see Fig. 2.4).

The magnitude of the co-polarized spatial frequency spectrum $|A_{\text{co}}(k_x, k_y)|$ computed for small and large sampling plane sizes are shown in Fig. 2.5. It exhibits several interesting features: (i) as expected, the dominant spectral component corresponds to the on-axis PW, for which $k_x = k_y = 0$, while the second strongest set of

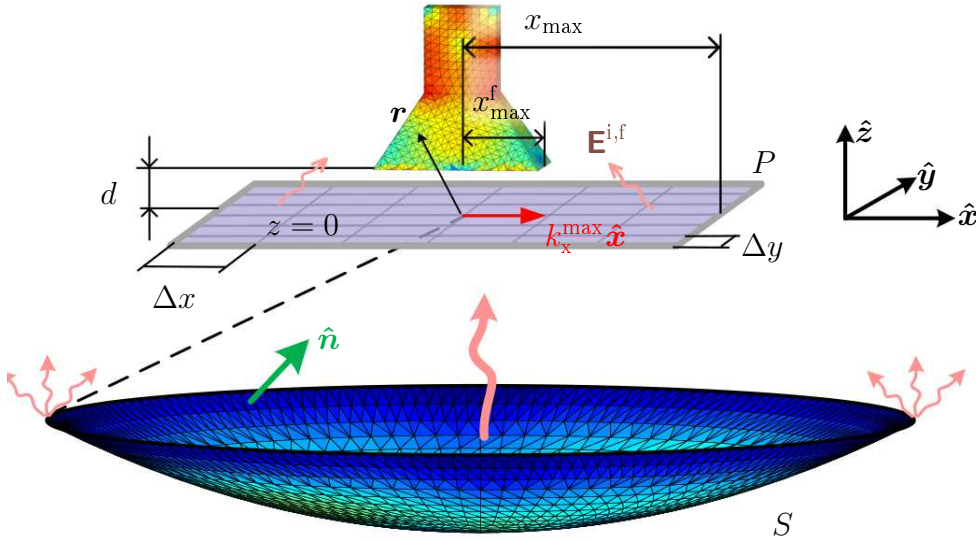


Figure 2.4: The FFT-enhanced PWS expansion method for the fast computation of the feed current due to the E -field from the reflector. Firstly, the incident field $\mathbf{E}^{\text{i,f}}$ is sampled in the xy plane P in front of the feed in order to obtain the sampled PWS $\mathbf{A}(k_x, k_y)$; Secondly, each spectral PW propagates to an observation point \mathbf{r} on the feed where $\mathbf{E}^{\text{i,f}}$ is tested to compute the induced feed current.

2.2. ACCELERATION TECHNIQUES

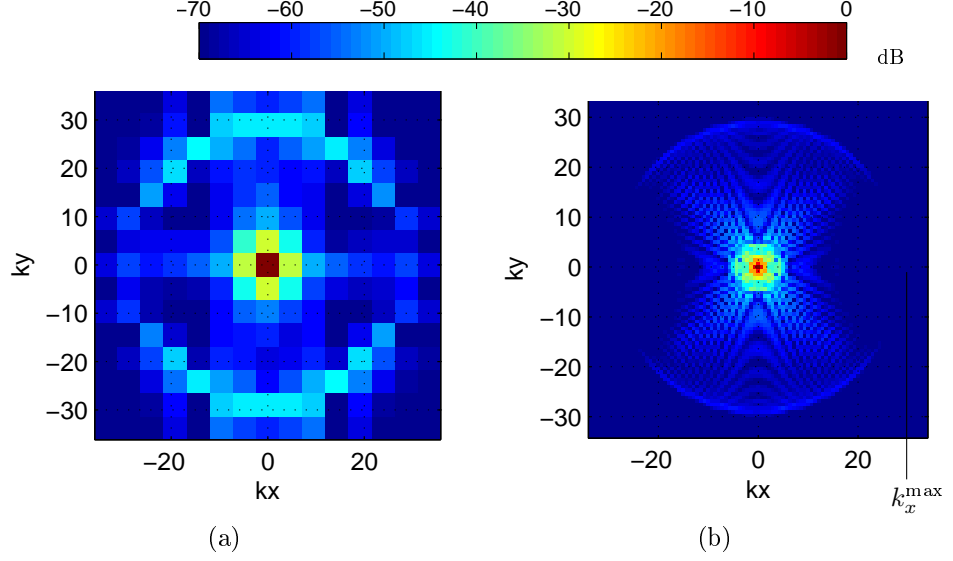


Figure 2.5: (a) The magnitude of the spatial frequency spectrum $|A_{\text{co}}(k_x, k_y)|$ (i.e. plane wave spectrum) for the 38λ reflector fed by the dipole array in case the FFT grid size is equal to size of the feed, and (b) when it is eight times the feed size.

PWs originate from the rim of the reflector, as observed by the spectral ring structure for which $k_x^2 + k_y^2 = (k_x^{\text{max}})^2 = (k_y^{\text{max}})^2$; (ii) the magnitude of the PWs originating from the rim is polarization dependent, in fact, it is seen that, since the feed is X -polarized, the feed field interacts more at the top and bottom segments of the rim.

The approximation of the reflector field by a PWS introduces an error, ϵ_1 , in the surface current of the feed. The relative error between the current expansion coefficient vectors $\mathbf{I}^{\text{approx}}$ and \mathbf{I}^{ref} for the iterative CBFM-PO solution with and without field approximations, respectively – is computed as

$$\epsilon_1 = \left(\sqrt{\sum_i |I_i^{\text{ref}} - I_i^{\text{approx}}|^2} / \sqrt{\sum_i |I_i^{\text{ref}}|^2} \right) \times 100\%. \quad (2.11)$$

Fig. 2.6 illustrates the relative error computed as a function of the FFT sampling plane size P when the PWS is employed for expanding the reflector radiated field (for PWS parameters see Paper 3), and when only the dominant on-axis PW term is used. As expected, the error decreases for an increasing sampling plane size, since more spectral PW terms are taken into account while the effect of the FFT-related periodic continuation of the spatial aperture field decreases. Henceforth, we choose the sampling plane size equal to that of the feed, for which the feed current error is about -35 dB for all the considered feeds, while it represents a good compromise from both a minimum number of sampling points and accuracy point of view. Conversely, if only the dominant on-axis PW term is used to approximate the reflector field, the error increases when the plane P becomes larger. This is due to the tapering of

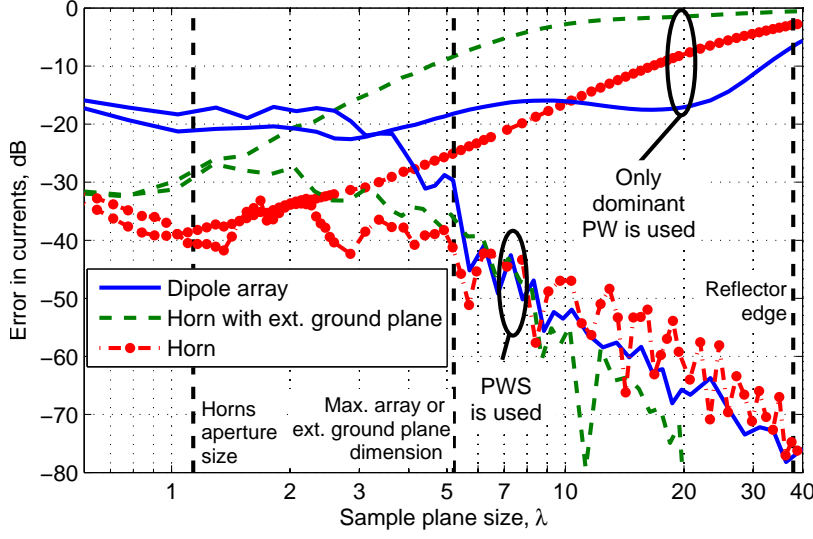


Figure 2.6: The relative error in induced feed currents [cf. (2.11)] as a function of the FFT sampling plane size P .

the reflector scattered field which becomes more pronounced when the plane size P increases, so that the PW amplitude $A(k_x, k_y)$ is underestimated when using the field averaging in (2.9a) for $k_x = k_y = 0$, as opposed to the direct on-axis point sampling method that has been presented in [37] and overviewed in Sec. 2.2.1.

2.2.3 Near-field interpolation (NFI) technique

While the previous section describes how the PWS-expanded E -field from the reflector accelerates the computation of the induced feed current, this section explains how the reflector incident H -field can be computed for the rapid determination of the induced PO current. For this purpose, the radiated H -field from the feed is first computed at a coarse grid on the reflector surface (white circles in Fig. 2.7), after which the field at each triangle is determined on the reflector (yellow square markers) through an interpolation technique. This interpolation technique de-embeds the initially sampled field to a reference sphere with radius R whose origin coincides with the phase center of the feed to assure that the phase of the de-embedded field will be slowly varying. Consequently, relatively few sampling points are required for the field interpolation, after which the interpolated fields are propagated back to the reflector.

In summary, and with reference to Fig. 2.7, the H -field interpolation algorithm for determining the reflector PO current

1. Defines a grid on the reflector surface (white circles) for computing the H -field.
2. De-embeds the H -field to a reference sphere around the feed phase center (green

2.2. ACCELERATION TECHNIQUES

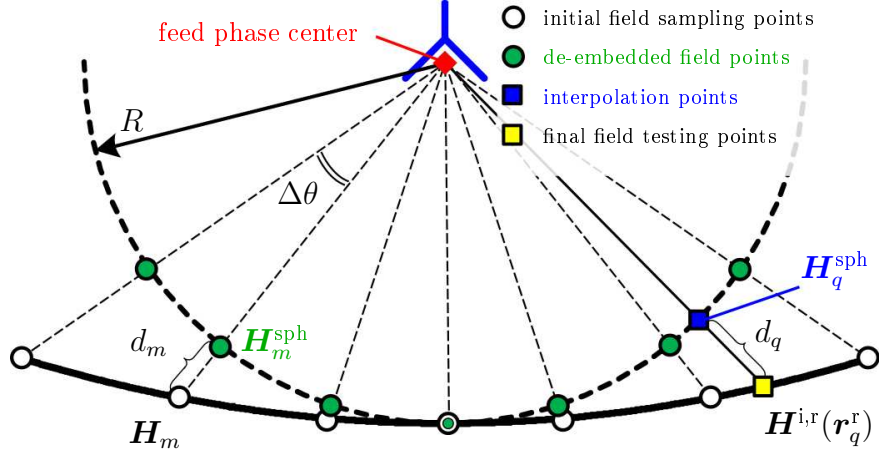


Figure 2.7: The near-field interpolation technique for the rapid determination of the induced PO current on the reflector.

points):

$$\mathbf{H}_m^{\text{sph}} = \mathbf{H}_m d_m e^{jkd_m}, \quad (2.12)$$

where d_m is the distance between the reflector surface and the sphere of radius R along the line connecting the m th sample point on the reflector and the feed phase center.

3. Computes the fields on the sphere in the same directions as the reflector triangle centroids are observed (blue square markers) through interpolating the fields at the adjacent (green) points.
4. Propagates the field to the reflector surface; that is, at the q th triangle, the H -field

$$\mathbf{H}^{i,r}(\mathbf{r}_q^r) = \mathbf{H}_q^{\text{sph}} d_q^{-1} e^{-jkd_q}. \quad (2.13)$$

5. Computes the reflector PO current (see e.g. [62, p. 343])

The error in the reflector current as a function of the sampling grid density is depicted in Fig. 2.8. It shows that the error in the resulting induced reflector current depends on the angular step size $\Delta\theta$ and $\Delta\phi$ of the initial field sampling grid (before interpolation). As expected, the error increases when the sampling grid coarsens. Furthermore, the error is larger for larger feeds, especially for high-scattering ones, for which the scattered fields (i.e. 2nd iteration and further) vary more rapidly than for smaller low-scattering antennas for which a coarser grid can be applied.

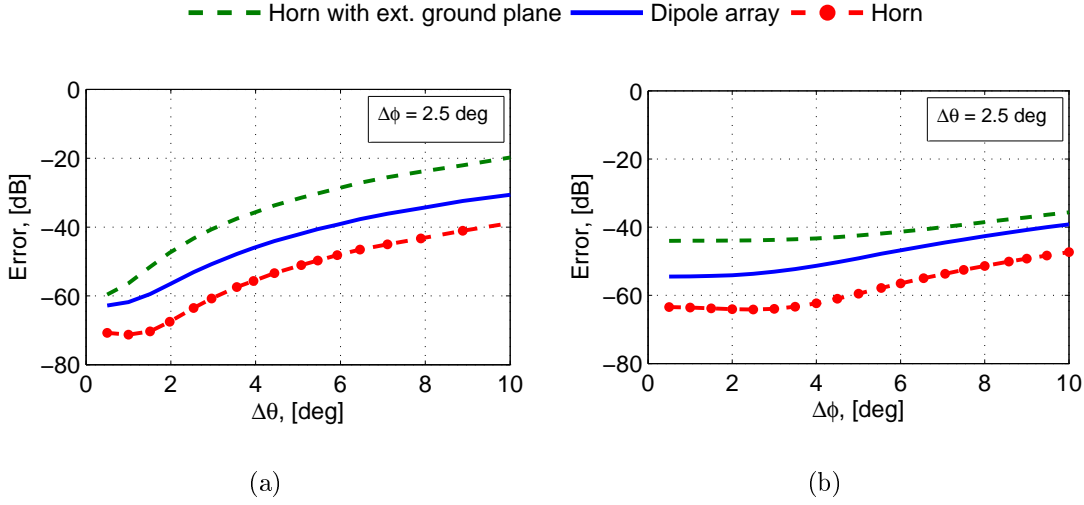


Figure 2.8: The interpolation error in the 38λ reflector current as a function of (a) the sampling step $\Delta\theta$, and (b) the sampling step $\Delta\phi$ of the near fields of the feed.

2.2.4 Analysis of PWE and NFI errors and simulation times

Table 2.3 shows how the simulation time of a “plain” iterative CBFM-PO (or MoM-PO) approach reduces, and Table 2.4 summarizes the relative errors in both the currents and relevant antenna characteristics when the field approximations of Sec. 2.2.1 are used. The errors have been computed according to (2.8) and (2.11). Note that the PWS approximation leads to the small relative error of 0.28% in the surface current of the high-scattering feed for the 38λ reflector, while if only a single on-axis PW is used, the relative error is found to be two orders larger (see Sec. 2.2.1). It is also observed that, when applying the field approximations for both the reflector and feed, the relative error in the considered antenna characteristics remains less than 1%, while the computational speed advantage is significant (see Table 2.3), i.e., a factor 5 to 100, depending on the reflector size and feed complexity.

Table 2.3: Total simulation time (for $D = 118\lambda$ reflector)

	Horn	Horn with ground plane	Dipole array	Vivaldi array
MoM-PO, no approx.	70 min (100%)	192 min (100%)	801 min (100%)	3906 min (100%)
PWS approx.	27 min (39%)	63 min (33%)	190 min (24%)	1312 min (34%)
NFI approx.	57 min (81%)	152 min (79%)	548 min (68%)	2108 min (54%)
Both approx.	13 min (19%)	17 min (9%)	16 min (2%)	33 min (1%)

Table 2.4: Errors due to applying the field approximations, %

	Feed surface current		Reflector surface current		Gain (on-axis)		Gain (@-3 dB)		Impedance	
Reflector	38 λ	118 λ	38 λ	118 λ	38 λ	118 λ	38 λ	118 λ	38 λ	118 λ

Feed: Pyramidal horn

PWS approx.	0.09	0.02	0.11	0.03	0.09	0.03	0.07	0.02	0.16	0.04
NFI approx.	0.01	<0.01	0.06	0.06	0.05	0.04	0.01	0.02	0.01	<0.01
Both approx.	0.09	0.02	0.13	0.07	0.13	0.07	0.07	0.04	0.15	0.04

Feed: Pyramidal horn with extended ground plane

PWS approx.	0.28	0.02	0.41	0.02	0.06	0.01	0.09	0.01	0.44	0.04
NFI approx.	0.3	0.01	1.01	0.16	0.16	0.07	0.37	0.07	0.52	0.02
Both approx.	0.53	0.03	1.02	0.16	0.15	0.08	0.34	0.07	0.88	0.05

Feed: 121-element dual-polarized dipole array

PWS approx.	0.05	0.02	0.1	0.02	0.03	0.01	0.01	0.01	0.03	0.01
NFI approx.	0.02	0.01	0.21	0.20	0.09	0.07	0.12	0.13	0.02	0.01
Both approx.	0.06	0.02	0.23	0.21	0.10	0.07	0.13	0.14	0.05	0.02

2.3 Experimental verification of the CBFM-PO approach with acceleration techniques

In addition to several cross-validations of the CBFM-PO approach using commercial software (see Paper 3), a practical antenna system has been modeled and the computed illumination efficiency η_{ill} is compared to measurements. Fig. 2.9 shows η_{ill} of a 118 λ reflector antenna ($D = 25$ m, $F/D = 0.35$), either fed by the Vivaldi array feed, or a single horn antenna. The numerically computed results are compared to measurements carried out at the Westerbork Synthesis Radio Telescope (WSRT) [7]. As one can see, the agreement is very good. The size of the simulated ground plane has been chosen equal to the size of the feed cabin ($\approx 1 \times 1$ m). The fact that η_{ill} is higher for the array feed than for the horn antenna nicely demonstrates the superior focal field sampling capabilities of dense PAFs. Furthermore, one can also observe a rather strong ripple in η_{ill} for the case of the horn feed with the extended ground plane. This ripple is caused by the relatively high feed scattering of the reflector field.

2.4 Numerical studies for different types of reflector antenna feeds

In this section several feeds are considered as part of a reflector antenna with aperture diameter 38 λ . Several antenna characteristics, such as the radiation pattern, the receiving sensitivity, and the aperture- and focal field distributions are analyzed using

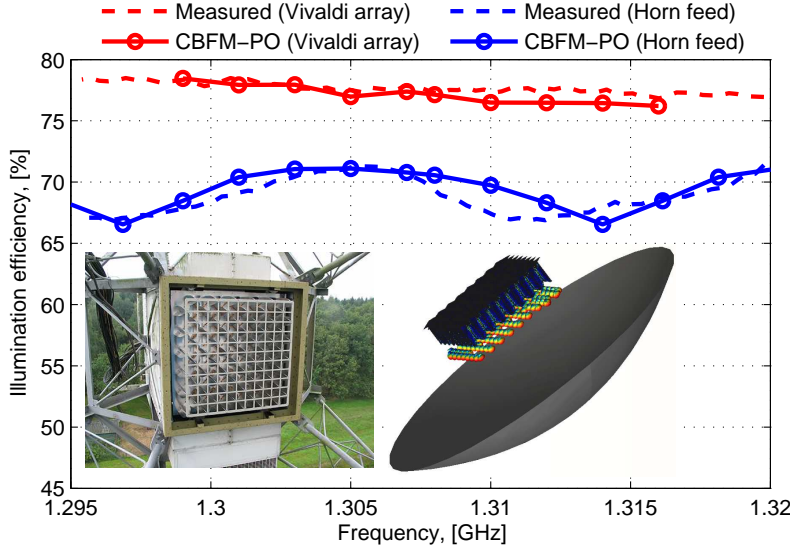


Figure 2.9: Illumination efficiencies of the 118λ reflector antenna, either fed by the 121 Vivaldi PAF, or the single-horn feed. The CBFM-PO simulated results are compared to the measured ones for a 25 m reflector antenna of the Westerbork Synthesis Radio Telescope [7]. Bottom of the figure: a photo of the experimental PAF system placed at the focal region of the reflector, and an image of a smaller-scale PAF-reflector model.

CBFM-PO approach. First, we will show how the feed-reflector coupling affects the field distribution in the aperture of the reflector when fed by the horn with extended ground plane or the dipole antenna array of the same size [see Fig. 2.3(b) and (c)]. Afterwards, the model of the antenna system will be extended to include the spillover and antenna-LNA noise mismatch characteristics, so that the receiving sensitivity can be analyzed.

The aperture field distributions at two frequency points corresponding to the minimum and maximum aperture efficiencies are shown in Fig. 2.10 and 2.11 for the horn and the dipole array feeds, respectively. It is pointed out that the antenna elements are loaded by a complex impedance, which is accounted for directly when solving for the antenna feed currents through the CBFM. This is done through the modification of the diagonal elements of the MoM matrix corresponding to the port basis functions as described in [54, p. 223]. The impedance of the loads has been chosen to maximize the array decoupling efficiency [52], which yields the optimum load impedance of $60.88 - 8.12j$ and $147.4 + 45.6j \Omega$ for the horn and array case, respectively. For the horn case this implies the ideal power-matched case.

As one can observe from the figures, the aperture field at the 2nd iteration, i.e., due to the scattered field of the feed [Fig. 2.10(c) and Fig. 2.11(c)], is about 20 dB lower for the array feed, thereby rendering the field variation negligible. Contrariwise, for the horn feed, the peak and dip of the field is clearly seen in the aperture center. This leads to a significant variation of the aperture efficiency η_{ap} over frequency, viz.

2.4. NUMERICAL STUDIES FOR DIFFERENT TYPES OF REFLECTOR ANTENNA FEEDS

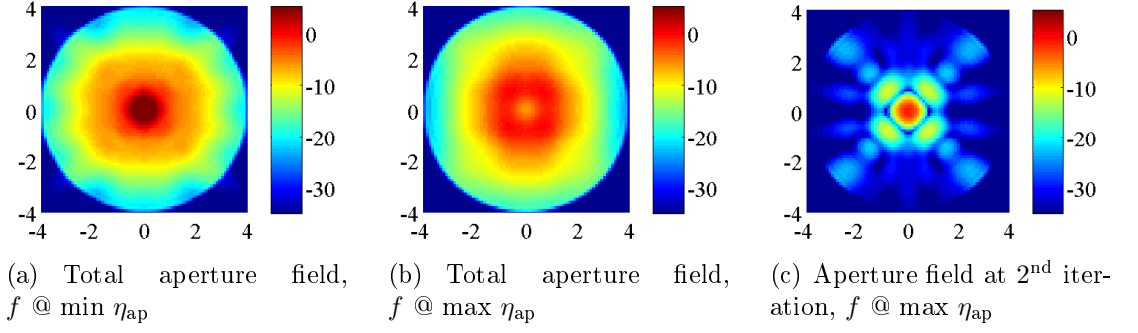


Figure 2.10: The field distribution in the aperture of 38λ -reflector fed by the horn with extended ground plane.

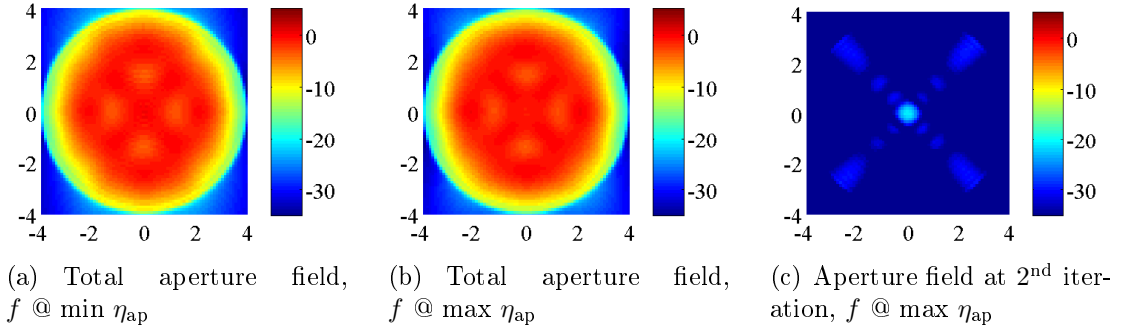


Figure 2.11: The field distribution in the aperture of 38λ -reflector fed by the array of 121 half-wavelengths dipoles.

19.6% versus 0.6% for the array.

For some applications, such as for radio astronomy, a reflector antenna works purely in receiving mode, and other system characteristics, such as the system noise temperature T_{sys} and the receiving sensitivity $A_{\text{eff}}/T_{\text{sys}}$, become important. The main contributors to T_{sys} , which are dependent on multiscattering effects, are the spillover noise temperature T_{spill} and the noise temperature due to the noise mismatch between the antenna(s) and LNA(s) ², T_{coup} . In order to compute T_{coup} , the equivalent one-port system representation is used as described in [63]. By using this extension to the CBFM-PO approach, the next step is to consider the two relatively small feeds shown in Fig. 2.12. The antenna array ports are connected to Low Noise Amplifiers (LNAs) which are also part of the antenna-receiver model. Two beamforming scenarios for the array are considered: (i) a singly-excited embedded element, and; (ii) a fully-excited antenna array employing the Conjugate Field Matching (CFM) beamformer for maximizing the gain of the secondary far-field beam.

The computed aperture efficiency η_{ap} , system noise temperature T_{sys} , and the resulting receiving sensitivity $A_{\text{eff}}/T_{\text{sys}}$ are shown in Fig. 2.13. By analyzing these

²in case of phased array feeds T_{coup} also takes the excitation scheme and coupling between the array elements into account.

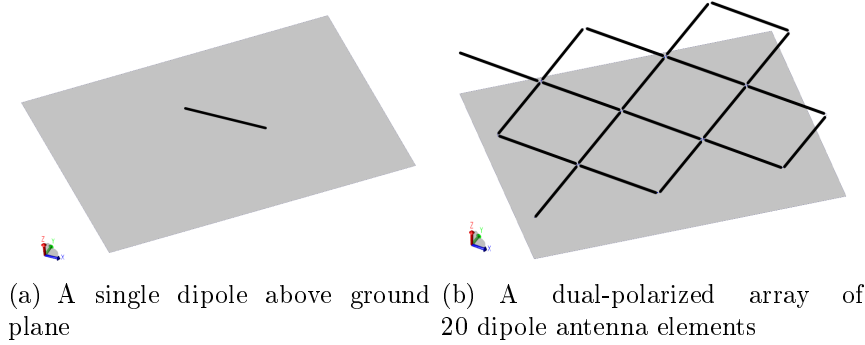


Figure 2.12: The considered dipole antenna feeds. The dipole length is (0.47λ) and the ground plane size is $(1.66\lambda \times 1.33\lambda)$

figures, one can conclude that the aperture efficiency varies with frequency much more for the case of a single element due to a fact that a lot of energy scatters from the ground plane behind the dipole.

The feed-reflector interaction phenomenon leads not only to the variation in η_{ap} , but also leads to a variation in T_{sys} . These variations are comparable for the the single dipole and array feeds, and have a major impact on the sensitivity ripple. Although T_{sys} is similar for both feeds, the mechanism of forming the ripple is different; when the reflector is fed by the feed shown in Fig. 2.12(a), the radiation pattern of the feed is “breathing” over frequency, resulting to the variation of the spillover noise temperature T_{spill} , while for the feed in Fig. 2.12(b) the main contribution to the T_{sys} variation is caused by the varying T_{coup} . See Paper 1 for more details.

2.5 Conclusions

To conclude the research that has been presented in this chapter, we highlight the following observations:

- The feed-reflector interaction (standing wave) effects give rise to oscillations in the system characteristics with frequency $\Delta f = c/(2F)$, where c is speed of light and F is the reflector focal distance. This results in the “heart beating” effect – the change of the beamwidth and gain, as well as T_{sys} variation over frequency.
- An FFT-enhanced Plane Wave Spectrum (PWS) approach has been formulated in conjunction with the Characteristic Basis Function Method, a Jacobi iterative multiscattering approach, and a near-field interpolation technique for the fast and accurate analysis of electrically large array feed reflector systems. Numerical validation (presented in Paper 3) has been carried out using the

2.5. CONCLUSIONS

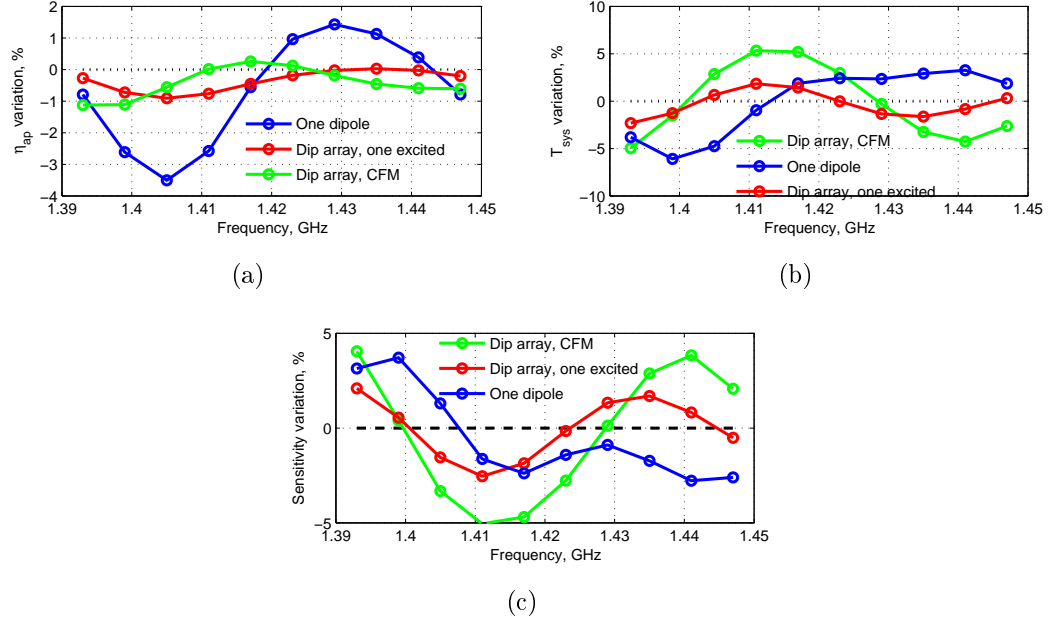


Figure 2.13: The aperture efficiency, the system noise temperature, and the resulting receiving sensitivity of the reflector antenna system as a function of frequency.

multilevel fast multipole algorithm method available in the commercial FEKO software.

- The scattering from the feed is minimal for power-matched antenna loads (more critical for PAFs) and when the surrounding metal structure is minimized (more critical for single-port feeds, especially in MFFEs).
- The electromagnetic coupling between the reflector antenna and the dipole PAFs under study have a minor impact on the antenna beam shape and aperture efficiency, as opposed to that of a single dipole feed. The finite ground plane behind the single dipole, which is part of the feed supporting structure and is often much larger than one antenna element, but comparable to the size of a PAF, is a reason for this difference.
- The (active) impedance matching of the strongly-coupled PAF elements appears to be more sensitive to the feed-reflector interaction effects, as a result of which the receiver noise temperature increases.
- The sensitivity variation is mainly driven by the variation in the system noise temperature, the main contribution of which for the considered PAF is due to the noise mismatch of the array elements with LNAs. Therefore, in order to reduce the sensitivity ripple of reflector antennas with PAFs, major attention

should be paid to the noise matching and its stability in the presence of a reflector when designing a PAF system.

- The conclusion in [41] which states that the Radar Cross-Section (RCS) of the feed is the determining factor in the standing wave effect is true only for the aperture efficiency variation, but it does not apply to the noise characteristics (T_{spill} , T_{coup}). Other factors showing why the RCS is not a good figure of merit to quantify the standing wave effect in receiving systems are that the the RCS does not account for the relative size of the feed w.r.t. the reflector, and that it assumes a uniform PW field radiated by the reflector.

Chapter 3

Phased Array Feed Beamforming Strategies for Earth Observations and Radio Astronomy

It has been argued in Sec. 1.2 that push-broom configurations for satellite radiometers are advantageous for Earth observation systems when equipped by PAFs. Therefore, the goals of the work presented in this chapter are to determine: (i) to what extent the performance-limiting factors of push-broom radiometers can be reduced by using dense PAFs employing advanced beamforming schemes; (ii) the minimum required complexity of the PAF design (size, number of elements and their arrangement in the feed as well as the number of active receiver channels), and (iii) what beamforming strategy to use for meeting the instrument specifications for future radiometers [10]. Finally, it will be shown how a constrained beamforming strategy can be used to improve the calibration efficiency of a radio telescope equipped by a PAF.

3.1 Application 1: Satellite radiometers for accurate ocean surveillance

3.1.1 Performance requirements

Before describing the push-broom array design and beamforming scenarios, the requirements for such radiometers are described first and how they are related to the antenna system requirements.

In February 2013 the ESA contract 4000107369-12-NL-MH was awarded to the team consisting of TICRA, DTU-Space, HPS, and Chalmers University. The first workpackage of the contract involved the review of ocean sensing performance parameters, which in turn resulted in the requirements for future satellite radiometers as shown in Table 3.1 [10, 64].

Table 3.1: Radiometer requirements

Freq., [GHz]	Bandwidth, [MHz]	Polarization	Sensitivity, [K]	Bias ΔT , [K]	Resolution FP, [km]	Dist. to land D_L , [km]
6.9	300	V, H	0.30	0.25	20	5-15
10.65	100	V, H	0.22	0.25	20	5-15
18.7	200	V, H	0.25	0.25	10	5-15

The table indicates that the radiometer should operate at three narrow frequency bands: C-band (6.9 GHz), X-band (10.65 GHz) and Ku-band (18.7 GHz). The instrument must be dual-polarized and have a receiving sensitivity in the 0.22 – 0.3 K range. The overall error of the sea temperature measurement should not exceed 0.25 K. The maximum allowed footprint size is 20 km for C- and X-band, and 10 km for the Ku-band. Under “footprint” we understand the region of the sea that is illuminated by the antenna beam from -3 to 0 dB level with respect to the beam maximum. Additionally, the instrument should satisfy the above described requirements even when the observation is as close as 15 km from the coast line. The latter requirement is called “distance to land” and explained with the aid of Fig. 3.1.

The brightness temperature of the land surface is assumed to be $T_L = 250$ K. Assume next that we wish to measure the sea at horizontal polarization for which the brightness temperature is around $T_H = 75$ K (the brightness temperature of the vertical polarization is higher, i.e. 150 K, and therefore it is less affected by the erroneous power signal from land). It can be shown that the requirement for the maximum error $\Delta T = 0.25$ K can be satisfied only if the power of the beam

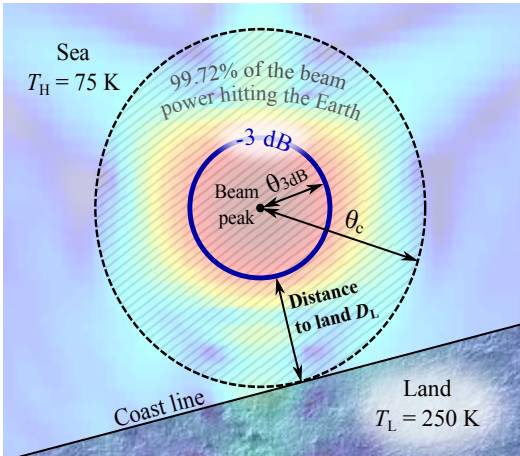


Figure 3.1: Definition of the “Distance to land” radiometer requirement. A typical radiation pattern of the torus reflector antenna is shown as background.

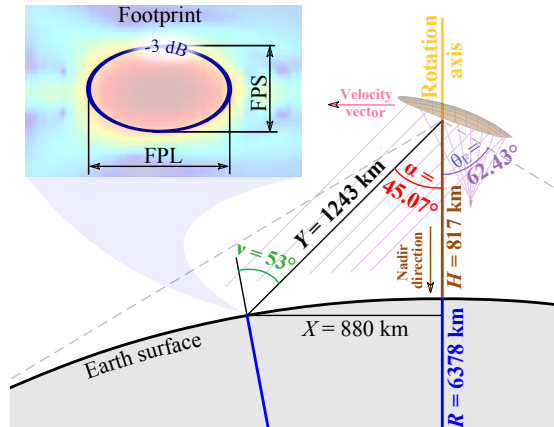


Figure 3.2: Geometrical parameters of the radiometer antenna system located on the Earth orbit. The notation of the major and minor axes of the footprint ellipse is shown in the top-left insertion.

3.1. APPLICATION 1: SATELLITE RADIOMETERS FOR ACCURATE OCEAN SURVEILLANCE

in the cone with half-angle θ_c is 99.72 % of the total power incident on the Earth's surface [31]. This determines the distance to land D_L , which is defined as the angular difference $\theta_c - \theta_{3\text{dB}}$ projected on the Earth surface, i.e.,

$$D_L = Y \sin \theta_c - Y \sin \theta_{3\text{dB}} \approx (\theta_c - \theta_{3\text{dB}})Y, \quad (3.1)$$

where Y is the distance from the satellite to the observation point on the Earth (see Fig. 3.2 for the satellite orbit parameters). Therefore, to find the distance-to-land characteristic, the angles θ_c and $\theta_{3\text{dB}}$ are found first from the antenna compound beam and Eq. (3.1) is used afterwards.

Since the radiometer must be able to measure the brightness temperature of both polarizations separately, an error is introduced due to the received power of the cross-polarized component of the incident field. It is shown in [31] that this power must not exceed 0.34 % of the co-polarized power, in order to satisfy the maximum error requirement $\Delta T = 0.25$ K. Since the brightness temperature of the sky is very low and the amount of power radiated towards the sky is small, it suffices to compute the antenna total radiation pattern only at the angular range subtended by the Earth ($\theta = 0 \dots \theta_E$ from the Nadir direction).

Another requirement for the radiometer is the sampling resolution which sets requirements on the maximum size of the footprint (FP). The footprint will have an elliptical shape due to oblique incidence of the radiated field on the Earth's surface as shown in the top-left insertion of Fig. 3.2. The longitudinal and transverse to the movement direction axes of the ellipse are denoted as FPL and FPS, correspondingly. The footprint size, FP, is determined as the average of FPS and FPL:

$$\text{FP} = \frac{\text{FPS} + \text{FPL}}{2}, \quad (3.2)$$

where FPS is related to the half-power beamwidth (HPBW) as

$$\text{FPS} = Y \times \text{HPBW}_{\text{transv}}, \quad (3.3)$$

and FPL is

$$\text{FPL} = \frac{Y \times \text{HPBW}_{\text{long}}}{\cos \nu}, \quad (3.4)$$

where $\text{HPBW}_{\text{transv}}$ and $\text{HPBW}_{\text{long}}$ are the longitudinal and transverse beamwidths to the movement vector directions; and ν is the incidence angle.

Another characteristic of the radiometer radiation pattern is the beam efficiency, which is usually defined as the relative power within the main beam down to the -20 dB contour level. A high beam efficiency is generally synonymous with a good quality antenna. However, a low beam efficiency antenna may not necessarily represent a bad antenna. For example, for the radiometer, the feed spillover past the reflector edge reduces the beam efficiency, but it illuminates the cold sky and does no harm; it is the radiation towards the Earth that makes a significant impact, and must therefore be taken in account.

3.1.2 Reflector antenna and PAF designs methodology

The initial numerical model of the PAF is based on the CBFM-model as described in [17]; the array elements are tapered-slot (Vivaldi) antennas designed to be employed as a PAF system [7]. The surface current distribution of the centrally excited Vivaldi array element is shown in Fig. 3.3(a) for illustration.

To reduce the computation time for the parametric studies, the PAF model has been simplified by assuming that all the embedded element patterns are identical to the central element of the finite array [Fig. 3.3(b)]. The sub-array embedded element patterns have been imported into the reflector antenna simulation software GRASP10 to compute the secondary embedded element patterns (after reflection from the dish), which, in turn, have been used to simulate the overall performance of the radiometer for optimizing its beamforming weights (see Sec. 3.1.3) as well as the array configuration.

The design procedure of the push-broom reflector is described in [33] and has been developed by TICRA. In short, and with the reference to Fig. 3.4, the surface of the reflector (blue dots) is created by rotation of the parabolic profile (black dots), defined in the coordinate system “Parabola CS” and with focal point F , around the green axis of rotation which is tilted with respect to the parabola axis. The reflector rim (edge of the red area) is chosen based on the requirements on the projected aperture area and maximum scan angle. The latter parameter also defines the size of the PAF along the focal arc, which is created by rotating the focal point F around the axis of rotation.

Due to the rotational symmetry of the reflector, it is natural to locate the array antenna elements in a polar grid with the origin located at the point where the axis

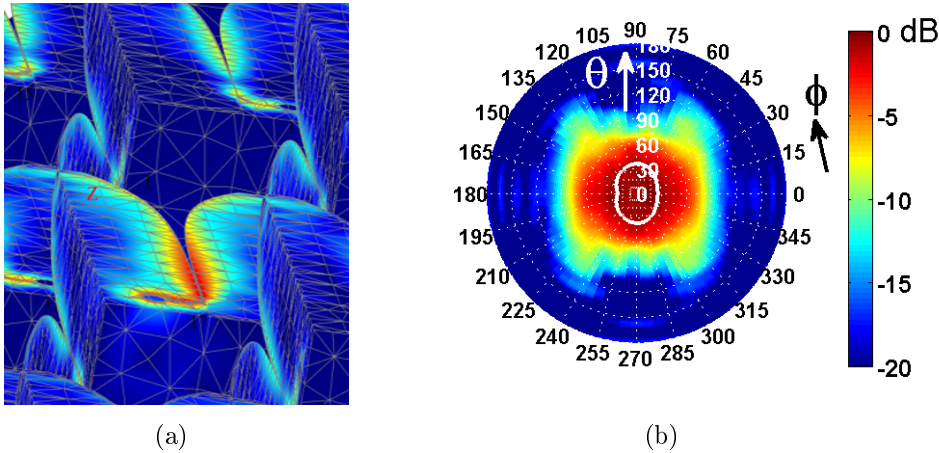


Figure 3.3: Simulation results of the finite Vivaldi array when the central antenna element is excited: (a) the magnitude of the surface current distribution in [dBA/m], and (b) the embedded element radiation pattern.

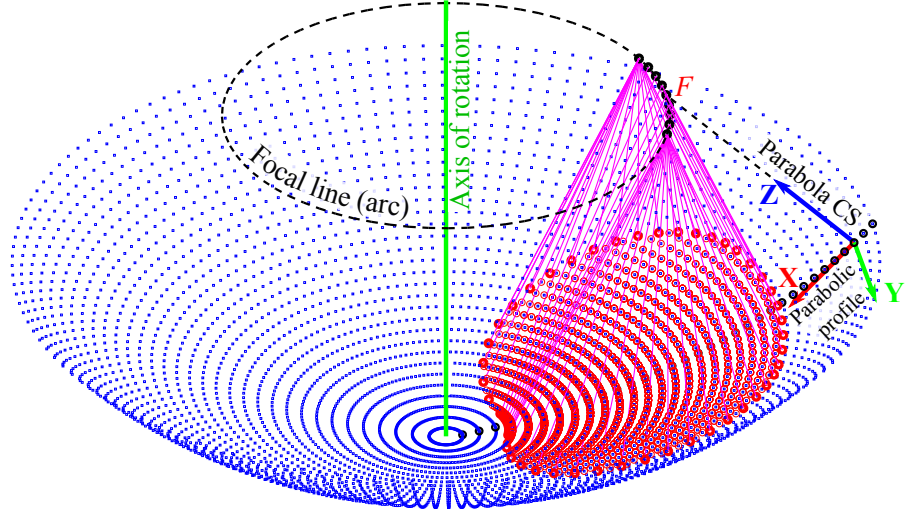


Figure 3.4: Design procedure of a parabolic torus reflector: the parabolic profile (black circles at the bottom), defined in the coordinate system “Parabola CS” and with focal point F , is rotated around the green axis of rotation which itself is tilted with respect to the parabola axis. This transforms the profile focal point F to the focal line (arc) along which a PAF will be positioned.

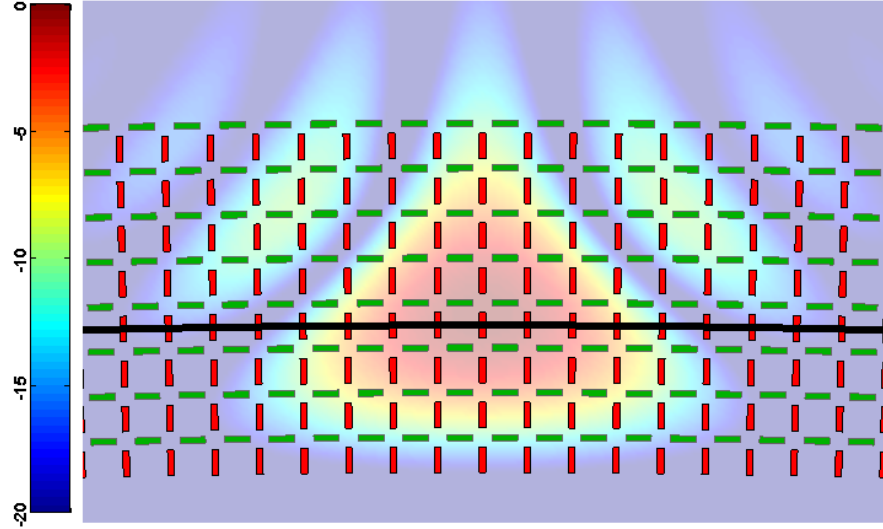


Figure 3.5: Layout of the PAF for the push-broom reflector: red and green lines denote the θ - and ϕ -polarized array elements correspondingly, while the black arc shows the position of the focal arc of the reflector. The E-field distribution in the array plane (when a tapered plane wave is incident on the reflector from the direction of observation) is shown as the background.

of rotation intersects the plane of the focal arc. The layout of such an array is shown in Fig. 3.5. The reflector focal arc is denoted by the black curve to show the position of the array relative to the reflector.

In order to choose the initial size of the array, a tapered plane wave is incident from the direction of observation on the reflector antenna and the vector EM field in the plane of the array is computed. The magnitude of the E-field is shown as the background in Fig. 3.5. The initial size of the array has been chosen such that it covers an area where the field intensity exceeds -20 dB, while the initial inter-element spacing has been chosen to be 0.5λ . This element spacing is expected to lead to a high beam efficiency, while minimizing the spillover loss [65]. The taper of the incident plane wave has been chosen -30 dB at the reflector rim. This value is shown to be optimal from the radiometer characteristics point of view [Paper 4], when the Conjugate Field Matching (CFM) beamforming is used. Since we will use more advanced beamformers, the focal field distribution will differ from the one shown in Fig. 3.5, so that the optimal array size can be different as well. This will be studied in Sec. 3.1.4.

3.1.3 Optimization procedure for the PAF beamformers

To outline the optimization procedure for the PAF beamformers considered in this work, we utilize the generalized system representation as shown in Fig. 3.6 for the N actively beamformed PAF antennas. The PAF system is subdivided into two blocks: (i) the frontend including the reflector, array feed and Low Noise Amplifiers (LNAs), and; (ii) the beamformer with complex conjugated weights $\{w_n^*\}_{n=1}^N$ and an ideal (noiseless/reflectionless) power combiner realized in software.

Here, $\mathbf{w}^H = [w_1^*, \dots, w_N^*]$ is the beamformer weight vector, H is the Hermitian conjugate-transpose, and the asterisk denotes the complex conjugate. Furthermore, $\mathbf{a} = [a_1, \dots, a_N]^T$ is the vector holding the transmission-line voltage-wave amplitudes

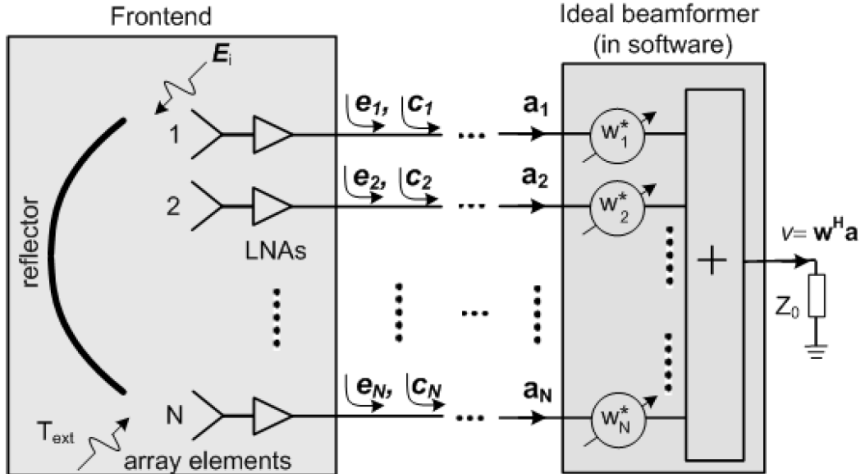


Figure 3.6: Generalized representation of the PAF reflector antenna system.

at the beamformer input (the N LNA outputs). Hence, the fictitious beamformer output voltage v (across Z_0) can be written as $v = \mathbf{w}^H \mathbf{a}$, and the receiver output power as $|v|^2 = vv^* = (\mathbf{w}^H \mathbf{a})(\mathbf{w}^H \mathbf{a})^* = (\mathbf{w}^H \mathbf{a})(\mathbf{a}^T \mathbf{w}^*)^* = \mathbf{w}^H \mathbf{a} \mathbf{a}^H \mathbf{w}$, where the proportionality constant has been dropped as this is customary in array signal processing and because we will consider only ratio of powers.

Although each subsystem can be rather complex and contain multiple internal signal/noise sources, it is characterized externally (at its accessible ports) by a scattering matrix in conjunction with a noise- and signal-wave correlation matrix. Accordingly, the signal-to-noise ratio (SNR) can be expressed as

$$\text{SNR} = \frac{\mathbf{w}^H \mathbf{P} \mathbf{w}}{\mathbf{w}^H \mathbf{C} \mathbf{w}}, \quad (3.5)$$

that is, the SNR function is defined as a ratio of quadratic forms, where $\mathbf{P} = \mathbf{e} \mathbf{e}^H$ is the signal-wave correlation matrix, which is a one-rank positive semi-definite matrix for a single point source; the vector $\mathbf{e} = [e_1, \dots, e_N]^T$ holds the signal-wave amplitudes at the receiver outputs and arises due to an externally applied electromagnetic plane wave \mathbf{E}_i ; and \mathbf{C} is a Hermitian spectral noise-wave correlation matrix holding the correlation coefficients between the array receiver channels, i.e., $C_{mk} = E\{c_m c_k^*\} = \overline{c_m c_k^*}$. Here, c_m is the complex-valued voltage amplitude of the noise wave emanating from channel m , which includes the external and internal noise contributions inside the frontend block in Fig. 3.6, and overbar denoted time average. We consider only a narrow frequency band, and assume that the statistical noise sources are (wide-sense) stationary random processes which exhibit ergodicity, so that the statistical expectation can be replaced by a time average (as also exploited in hardware correlators).

Below, we will first discuss two standard signal processing algorithms, which are then used as the starting point to develop the two customized push-broom radiometer beamformers.

Standard maximum signal-to-noise ratio (MaxSNR) beamformer

The well-known closed-form solution that maximizes (3.5) for the point source case, where \mathbf{P} is of rank 1, is given by [66]

$$\mathbf{w}_{\text{MaxSNR}} = \mathbf{C}^{-1} \mathbf{e}, \text{ with } \text{SNR} = \mathbf{e}^H \mathbf{w}_{\text{MaxSNR}}, \quad (3.6)$$

where the principal eigenvector \mathbf{e} corresponds to the largest eigenvalue of \mathbf{P} . If we assume a noiseless antenna system, the matrix \mathbf{C} will contain the noise correlation coefficients only due to external noise sources (received noise), and its elements can be calculated through the pattern-overlap integrals between $\mathbf{f}_n(\Omega)$ and $\mathbf{f}_m(\Omega)$, which are the n th and m th embedded element pattern of the array, respectively [17], i.e.,

$$C_{mn} = \int T_{\text{ext}}(\Omega) [\mathbf{f}_m(\Omega) \cdot \mathbf{f}_n^*(\Omega)] d\Omega, \quad (3.7)$$

where $T_{\text{ext}}(\Omega)$ is the brightness temperature distribution of the environment. The proportionality constants between the right-hand side and the noise waves on the left-hand side are omitted.

Standard Conjugate Field Matching (CFM) beamformer

The CFM beamformer maximizes the received signal power at its output, i.e., $\max_{\mathbf{w}}(\mathbf{w}^H \mathbf{P} \mathbf{w} / \mathbf{w}^H \mathbf{w})$, which is also equivalent to maximizing the directivity. The trivial solution to that is (provided that $\mathbf{P} = \mathbf{e} \mathbf{e}^H$)

$$\mathbf{w}_{\text{CFM}} = \mathbf{e}. \quad (3.8)$$

However, since this beamformer assumes a noiseless system, it will provide a sub-optimal solution for practical systems.

A customized MaxSNR beamformer with side-lobe level constraints

A major drawback of the above-listed standard beamformers is that these maximize the sensitivity/directivity without constraints imposed on the side-lobes and cross-polarization levels. This means that the required values of the distance-to-coast and the maximum allowable cross-polarization power cannot be guaranteed, especially for a non-parabolic surface of the reflector.

To overcome this limitation one could consider a tapered incident plane wave emitted by the source of interest with the taper value as an additional CFM beamformer parameter that is to be determined through a study. This has been done by our co-authors in Paper 4. Although the radiometer characteristics will then satisfy the system performance specifications, the PAF requires us to employ too many antenna elements (almost a factor 2 as compared to the customized beamformer [Paper 4]), which is not feasible for a realistic satellite system due to an excessive power consumption.

The MaxSNR beamformer has been used to maximize the beam efficiency (defined at the -20 dB level), while minimizing the power received from other directions in the presence of a noisy environment (including the noise sources due to the LNAs and the environment) and RFI sources in the region occupied by the Earth. For this purpose, the matrix \mathbf{C} in (3.6) has been modeled as a sum of noise covariance matrices due to LNAs and the environment brightness temperature $T_{\text{ext}}(\Omega)$ in (3.7), where the latter has been defined as a noise-mask-constraint function allowing to keep the peaks of the side-lobes below a specified level. This noise mask (Fig. 3.7, top-left insertion) is defined in the coordinate system for the secondary embedded element patterns and has zero temperature in the region of the main lobe and high temperature in the region of side lobes. A temperature of 1000 K is chosen to highly suppress the side lobes in order to satisfy the “distance-to-coast” requirement. This

value, as well as size and shape of the “cold” region, can also be beamformer optimization parameters, which is planned to be done in future studies. The noise mask is specified for each beam of the radiometer (pink rays in Fig. 3.7).

The customized MaxSNR beamformer with constraints on the dynamic range of the amplitude weights

The customized beamformer, as described above, has been further extended so as to include constraints on the dynamic range of the weights. This beamforming algorithm is implemented through an iterative procedure that modifies the reference weighting coefficients (as determined by the customized beamformer as described above), while trying to maintain the shape of the PAF pattern as close as possible to the reference one. This will ensure that the radiometer parameters are as close as possible to those obtained with the reference set of weights. The corresponding algorithm is listed as follows:

- At the first iteration ($q = 1$) the sensitivity function $\frac{[\mathbf{w}^{(1)}]^H \mathbf{P} \mathbf{w}^{(1)}}{[\mathbf{w}^{(1)}]^H \mathbf{C}^{(1)} \mathbf{w}^{(1)}}$ is maximized

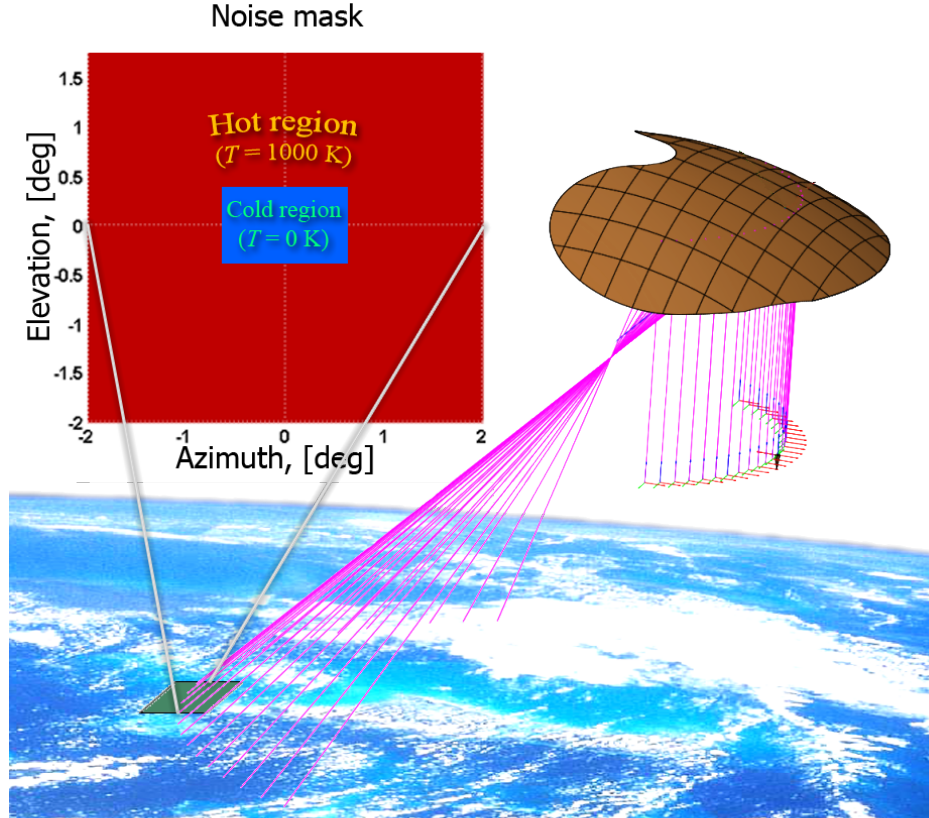


Figure 3.7: Noise mask definition for the MaxSNR beamforming.

to determine the reference weight vector $\mathbf{w}^{(1)}$. The matrix $\mathbf{C}^{(1)}$ is computed as described above for the standard MaxSNR beamformer (with no constraints on the dynamic range of the weight amplitudes).

- At iteration $q = 2, 3 \dots$ the sensitivity function $\frac{[\mathbf{w}^{(q)}]^H \mathbf{P} \mathbf{w}^{(q)}}{[\mathbf{w}^{(q)}]^H \mathbf{C}^{(q)} \mathbf{w}^{(q)}}$ is maximized to determine the new weight vector $\mathbf{w}^{(q)}$, where \mathbf{P} is the signal covariance matrix (computed only once, for the 1st iteration), $\mathbf{C}^{(q)}$ is the noise covariance matrix, diagonal elements of which are a function of the weight vector $\mathbf{w}^{(q-1)}$ obtained after the previous iteration, i.e.,

$$\mathbf{C}^{(q)}(\mathbf{w}^{(q-1)}) = \begin{bmatrix} C_{11}^{(q-1)} f(|w_1^{(q-1)}|) & C_{12}^{(q-1)} & \dots & C_{1N}^{(q-1)} \\ C_{21}^{(q-1)} & C_{22}^{(q-1)} f(|w_2^{(q-1)}|) & \dots & C_{2N}^{(q-1)} \\ \vdots & \vdots & \ddots & \vdots \\ C_{N1}^{(q-1)} & C_{N2}^{(q-1)} & \dots & C_{NN}^{(q-1)} f(|w_N^{(q-1)}|) \end{bmatrix}, \quad (3.9)$$

where f is a receiver function that needs to be provided as an input to the algorithm; it should have such a behaviour that the lower the weight of the array antenna element, the higher the function value is (which physically corresponds to an increase in the noise temperature of the corresponding receiver channel). In the numerical examples presented hereafter, a filter function is used whose values are close to zero when the weights magnitude $|w_i|$ are higher than w_{constr} , and which has a sharp linear increase near w_{constr} . In this way f is similar to inverse step function near w_{constr} (Fig. 3.8). Here w_{constr} is the value of the amplitude weight constraint, which is typically in the order of -30 dB or -40 dB.

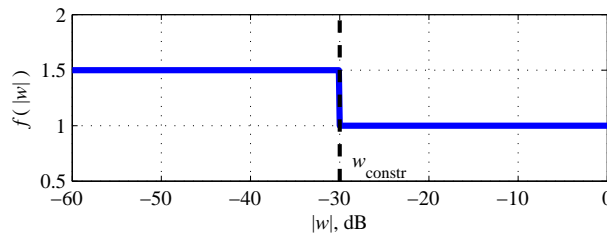


Figure 3.8: The function f used in the numerical examples presented hereafter.

- Check whether all the weights are higher than w_{constr} , or negligibly low (i.e. -80 dB in this work). If this condition is satisfied, the iterative procedure is terminated. The channels with negligible weights are switched-off, while the resulting set of weight coefficients is considered to be the final one.

3.1.4 Numerical results: Optimized PAF+beamformer design

The initial array layout obtained in Sec. 3.1.2 will not be the optimal one for different beamforming scenarios since these beamformers form different focal field distributions, and therefore we may need more, or less, antenna array elements to sample this field sufficiently to satisfy the radiometer requirements. Under “optimal array” we understand an array employing a minimum number of antenna elements, while all performance requirements of the radiometer equipped with a such array remain satisfied.

Effect of the array size and inter-element spacing on radiometer characteristics

To optimize the initial array layout in conjunction with the customized beamformers described in the previous sections, the main characteristics of the radiometer are studied as a function of the inter-element spacing between the array elements and the array size in the radial direction. The array size in the azimuthal direction is not a parameter of interest in the optimization, since the array will be needed to form multiple beams in this direction and sub-arrays for the neighbouring beams will overlap. This work is presented in Paper 5, while the performance of the radiometer at the X-band is summarized in Table 3.2. In this case the radiometer is subsequently equipped with: (i) a horn feed (radiation pattern of which is modeled as a Gaussian beam), (ii) the initial array with the CFM beamformer, (iii) the initial array employing the customized MaxSNR beamformer (unconstrained dynamic range of the amplitude weights), and; (iv) the optimized array feed with the latter beamformer.

As expected, dense PAFs have obvious benefits in achieving the required minimum distance-to-coast and footprint roundness, while meeting all the other radiometer requirements at the same time. The minimum size of the PAF sub-array has been found to be 8×21 elements (for each polarization) with the inter-element separation distance in the order of $d_{\text{el}} = 0.7\lambda$.

Effect of weights dynamic range on radiometer characteristics

It is assumed in the above presented study that the dynamic range of the weight amplitudes is infinite, which is impossible for a real system. In order to investigate how the limitation on the dynamic range of weights affects the radiometer performance, the customized MaxSNR beamformer with constraints on the dynamic range of the weights has been used and the radiometer characteristics have been computed as a function of w_{constr} (see description of this beamformer in the previous section). The results are shown in Fig. 3.9 for two types of array elements: a wide-band Vivaldi antenna (solid curve), and a narrow-band antenna modelled by a Gaussian beam (dashed curve). The PAF of Vivaldi antennas will be referred to as “Feed 1” and the

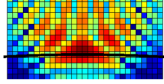
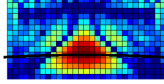
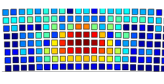
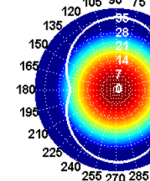
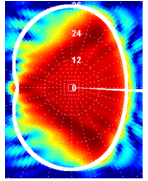
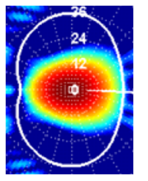
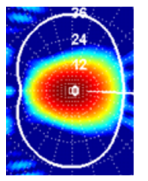
	Gaussian feed model	PAF with CFM-BF $15 \times 29 \times 2$ elem. $d_{el} = 0.5\lambda$	PAF with Cust-BF $15 \times 29 \times 2$ elem. $d_{el} = 0.5\lambda$	PAF with Cust-BF $8 \times 21 \times 2$ elem. $d_{el} = 0.7\lambda$
PAF element excitation coefficients				
Reflector illumination patterns				
Beam efficiency [%]	84.2	85.1	94.9	92.0
XP-power, [%] ($<0.34\%$ is req.)	0.39	1.01	0.03	0.02
Dist. to land, [km] (<15 km is req.)	87.8	116.6	14.0	15.9
Beam width, [deg]	0.600	0.351	0.512	0.538
Footprint (FP), [km] (<20 km is req.)	16.9	10.5	14.4	14.9
FP ellipticity	1.38	2.14	1.33	1.22

Table 3.2: Radiometer characteristics for different PAFs and beamformers

PAF of Gaussian beams will be called “Feed 2”.

Having analyzed the figure, one can conclude the following:

- The beam efficiency [Fig. 3.9(a)] is high for “Feed 1” when the dynamic range of the weights exceeds 30 dB, while for the “Feed 2” it remains high for all considered values of w_{constr} . The reason for this difference is that a Vivaldi antenna tends to have significant side radiation in comparison with an ideal Gaussian beam model, which leads to higher spillover towards the cold sky and, therefore, reduces the beam efficiency while keeping the distance to land sufficiently small.
- The distance to land [Fig. 3.9(b)] is similar for both PAFs. “Feed 2” is slightly better due to the fact that the Gaussian beam is a rotationally symmetric smooth function, which simplifies the formation of a PAF beam for such antennas.
- The footprint size [Fig. 3.9(c)] is almost identical for both PAFs. A little difference in the footprint ellipticity (FPL/FPS) is observed when the weight dynamic range is around 20 dB or less. The reason for this is the same as for the “distance-to-land” result.

- Regarding the power in the cross-polarized field component, “Feed 1” can compete with the “Feed 2” when the weight dynamic range exceeds ~ 38 dB. Since the Gaussian beam itself does not have a cross-polarized component, the values observed in Fig. 3.9(d) are due to the field radiated by the feed and scattered from the toroidal reflector. Therefore, the following important conclusion can be drawn: in order to satisfy the cross-polarization requirement, and if the maximum allowed dynamic range is less than ~ 35 dB, the antenna elements in the array must illuminate the reflector with low cross-polarized field power.

The weight coefficients, the reflector illumination patterns, and the secondary patterns for the constraint levels -40 dB; -30 dB; and -20 dB are shown in Fig. 3.10.

Unfortunately, the antenna pattern resulting from the 20 dB range beamformer suffers from higher side-lobe and cross-polarization levels. The 30 dB range beamformer requires ~ 12 % less elements than the 40 dB beamformer, but leads to an almost identical antenna beam shape.

Since it is technically feasible to reach a dynamic range of 30 dB [67], this dynamic range value has been chosen for the constrained beamformer used in the final design of the array. In addition, a narrow-band antenna element with low cross-polarization level will be used for the PAF to satisfy the cross-polarization power requirement.

Final array design and radiometer characteristics

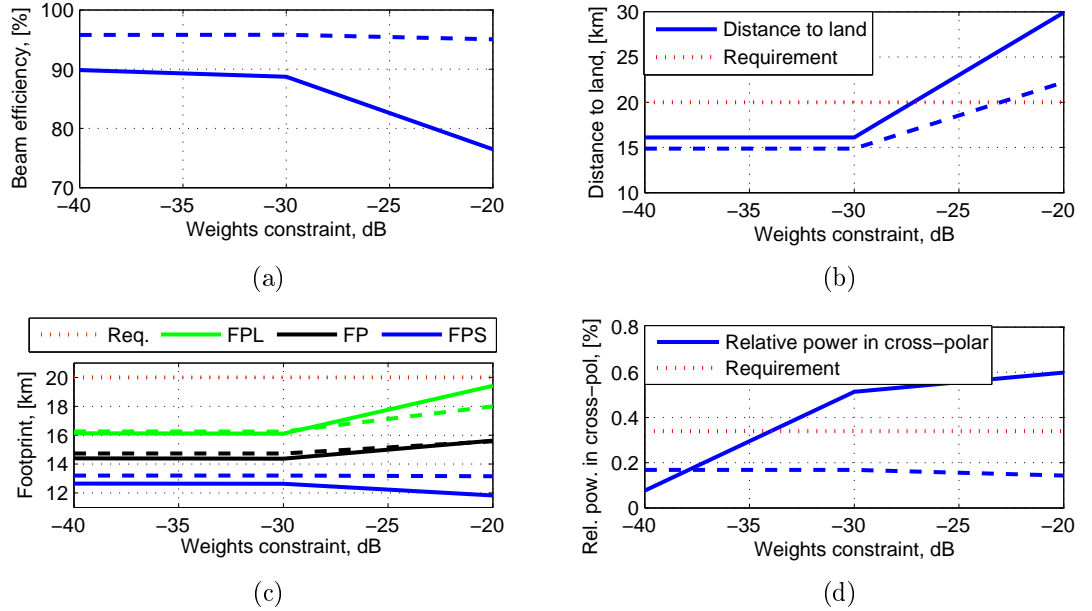


Figure 3.9: The radiometer characteristics as a function of the dynamic range of the weights. The results are shown for two array element types: a wide-band Vivaldi antenna (solid curve) and a narrow-band antenna modelled by a Gaussian beam with the same taper on the edge of the reflector (dashed curve).

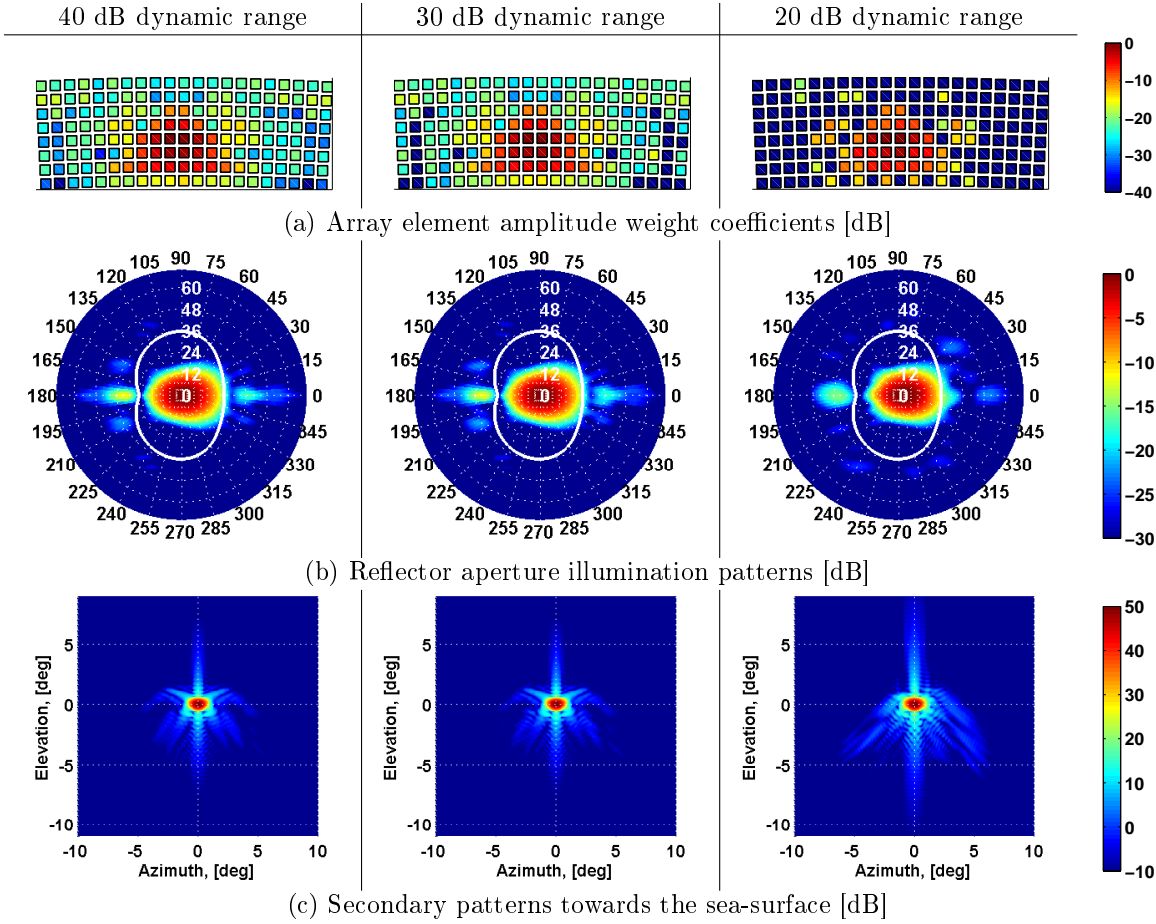


Figure 3.10: Comparison of three realizations of the customized MaxSNR beamformer with the dynamic range of amplitude weights of 40, 30 and 20 dB. The PAF elements are Gaussian beams.

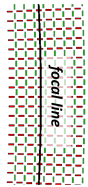
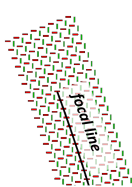
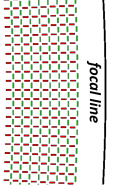
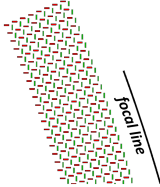
For operation at C-, X and Ku bands, we have considered the use of three radial PAFs (one for each band) with their respective locations in the focal region of the reflector antenna, as illustrated on Fig. 3.11. The PAF at Ku band is placed along the focal line, while the C- and X-band PAFs have off-set locations.

Since, the off-set location of the antenna feed can cause degradation of the antenna pattern and increase of the side-lobe levels, we have re-evaluated the performance of the optimized PAF design for this case. Table 3.3 cross-compares the resultant radiometer characteristics for the on-axis and off-set PAFs, both for the center and most scanned beams. As one can see, the effect of the expected degradation due to an off-set location is negligible, and therefore, no additional corrections to the previously optimized PAF design are required.

Radiometer characteristics for the radial PAFs at C-, X and Ku-band for the case of the center beam are shown in Table 3.4 (the performance of scanned beams is similar). It is seen from the table that all requirements for the radiometer are either

3.1. APPLICATION 1: SATELLITE RADIOMETERS FOR ACCURATE OCEAN SURVEILLANCE

Table 3.3: Effect of off-set location of PAF with respect to the focal line at X-band

	Axial location w.r.t. focal line		Off-set location w.r.t. focal line	
	centre beam 	20° scan beam 	centre beam 	20° scan beam 
Beam efficiency @ -20 dB, [%]	92.02	90.96	90.04	90.62
Distance to land, [km]	15.8	15.7	16.1	15.9
Footprint, [km]	14.9	15.3	14.4	14.8
FPL[km] / FPS[km]	16.4/13.4	16.4/14.2	16.1/12.6	16.1/13.4
Ellipticity	1.22	1.16	1.27	1.21
Relative cross-polar level, [%]	0.021	0.098	0.028	0.073
Directivity, [dB]	50.81	50.58	51.12	50.96
Beam width, ($\phi = 0 \times \phi = 90$) [deg]	0.62×0.46	0.65×0.46	0.58×0.45	0.62×0.45
Power hitting reflector, [%]	93.06	92.02	91.08	91.68

satisfied or very close to them. Further improvement can be made by adjusting the noise mask used in beamforming (see Fig. 3.7). This will be done in future studies. The low beam efficiency at X- and Ku-band is due to spillover towards the cold sky, and therefore it does not affect the radiometer performance.

Since the radiometer is supposed to perform measurements with multiple beams,

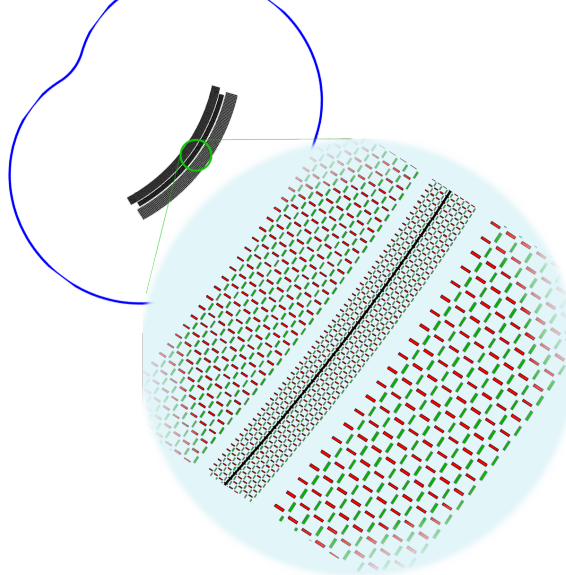


Figure 3.11: (from left to right) X-, Ku- and C-band PAFs in the push-broom reflector antenna system.

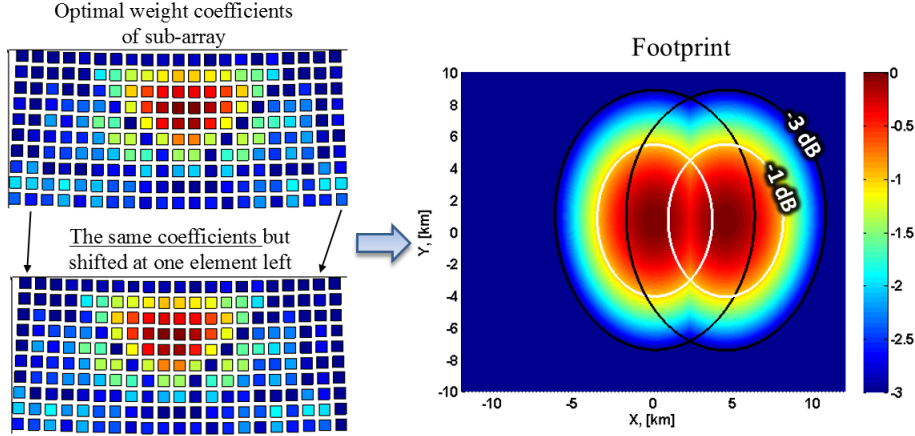
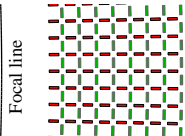
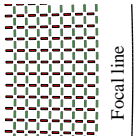
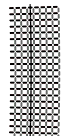


Figure 3.12: (left) Array element amplitude weight coefficients [dB], for two sub-arrays: for the center beam and for the 1st scanned beam; and (right) corresponding footprint patterns [dB].

these beams should satisfy Nyquist's sampling criterion, i.e., the distance between maximums of the neighbouring beams should not exceed half of the half-power beamwidth. We have conjectured above that the same set of weights can be applied to the different sub-arrays for forming the scanned beams. To check how well the closest beams are overlapped we shift the optimal weights (obtained for the on-axis beam) by one element in the azimuthal direction and observe how well the new beam will overlap with the original one. The results of this numerical experiment are shown in Fig. 3.12. As one can see, the two overlapping beams resulting from the center sub-array and the 1st off-set sub-array realize a beam separation close to half of the half-power beamwidth and therefore satisfies Nyquist's sampling criterion.

The total number of single-polarized antenna elements in the various arrays are: 1776 at C-band, 2448 at X-band, and 4368 at Ku-band. The radiometer equipped

Table 3.4: Radiometer characteristics for the radial PAFs at C-, X and Ku-band for the case of the center beam

	C-band	X-band	Ku-band
			
Beam efficiency @ -20 dB, [%]	94.8	90.1	85.9
Distance to land, [km]	18.1	16.1	13.9
Footprint, [km]	20.5	14.4	8.9
Relative cross-polar level, [%]	0.025	0.03	0.02
Directivity, [dB]	48.3	51.1	55.1
Average beam width, [deg]	0.73	0.52	0.32

with such arrays will be able to form hundreds of simultaneous beams capable to provide a scan range of ± 20 deg, corresponding to a swath width of 600 km. However, this is a huge number of antenna elements for a satellite system. In fact, assuming an estimated power consumption of 1.38 W per receiver, using present state-of-the-art components [68], and since the number of receivers is 8592, this results in a unrealistically large total power consumption of 11.8 kW. However, in a 5-years time frame the power budget per receiver is estimated to be about 35 mW [68], which leads to a total power consumption of the whole front-end of only about 300 W.

3.2 Application 2: Radio telescopes for wide field-of-view sky surveys

In this section we will come back to the radio astronomy application of phased array feeds and show how a constrained beamformer may simplify the calibration of a beam shape.

Calibration of radio telescopes requires accurate models of the instrumental parameters and propagation conditions that affect the reception of radio waves [26]. These effects vary over time and the model parameters have to be determined at the time of observation through a number of calibration measurements. Furthermore, the calibration measurements should complete in a relatively short time and may be repeated often over the course of an observation during which the instrumental and atmospheric conditions can change significantly. One of the instrumental parameters that needs accurate characterization is the radiation pattern of the antenna, which is especially challenging in the arena of future array based multiple beam radio telescopes [69–71], both due to the complexity of these instruments, as well as the increased size of the Field-of-View (FoV). Calibrating for the radiation pattern of a multi-beam PAF-based radio telescope largely depends on the accuracy of the pattern model, and the availability of suitable reference sources to solve for the unknown parameters in the pattern model.

The proposed idea on improving the calibration efficiency of a radio telescope radiation pattern is to conform the beamformed far-field patterns to a two-parameter physics-based analytic reference model through the use of a linearly constrained minimum variance (LCMV) beamformer. Through this approach, which requires only a few calibration measurements, an accurate and simple pattern model is obtained.

The first term of the Jacobi-Bessel (*JB*) series solution of reflector antenna far field patterns [72, 73] is used as a reference pattern:

$$F_A(\theta, \phi) \propto \frac{J_1(ka \sin \theta)}{ka \sin \theta} \equiv \text{jinc}(ka \sin \theta), \quad (3.10)$$

where a is the reflector aperture radius; k is the free space wavenumber. This model has been extended to account for a beam width (parameter s in the equation below)

and the phase gradient of a scanned beam (parameter Ψ):

$$F(s, \Psi; \theta, \phi) = \text{jinc}(ksa \sin \theta) e^{j\Psi \sin \theta \cos(\phi - \phi_0)}, \quad (3.11)$$

in which s and Ψ control the the amplitude and phase distributions of the reference pattern, respectively.

The reference pattern (3.11) is used to define directional constraints in a LCMV beamformed PAF, for which the weights applied to the elements of the PAF are calculated according to [74] [66, p. 526]

$$\mathbf{w}_{\text{LCMV}}^H = \mathbf{g}^H [\mathbf{G}^H \mathbf{C}^{-1} \mathbf{G}]^{-1} \mathbf{G}^H \mathbf{C}^{-1} \quad (3.12)$$

in which \mathbf{x}^H means the complex conjugate transpose of \mathbf{x} , \mathbf{C} is the noise covariance matrix, \mathbf{g} is the constraints vector, and \mathbf{G} is the directional constraint matrix. For L elements in the array and constraints enforced in the K different directions $\{\Omega_1, \Omega_2, \dots, \Omega_K\}$, \mathbf{G} is an $L \times K$ matrix in which the i th column contains the signal response vector of the array due to a plane wave incident from direction Ω_i , and the corresponding element g_i in the vector \mathbf{g} is the constraint value enforced on the pattern in that direction. The choice of these constraint parameters comes from the reference pattern (3.11).

An effect of the model parameters s and Ψ on the resulting beam characteristics (directivity, side-lobes level) and the error between the actual LCMV beamformed pattern and its model (3.11) are presented in Paper 6, where the APERTIF PAF [7] has been used to feed an offset Gregorian reflector based on the MeerKAT radio telescope reflector antenna [75].

It is shown in Paper 6 that this beamforming approach has several performance benefits including circularly symmetric scanned beams over a wide FoV, even for non-symmetric reflector antennas. For the example of the MeerKAT offset Gregorian antenna, this strategy resulted in multiple beams with aperture efficiency above 70 % that could be approximated down to the 10 dB level as a single analytic function with an error of less than 5 %. In comparison with a conventional MaxDir beamformer, this would reduce the average pattern calibration model error by more than 50 %.

3.3 Conclusions

The major part of this chapter has been devoted to improving satellite radiometers for the remote sensing of the sea surface by employing a phased array feed together with the parabolic torus reflector. This is a first stage of the new radiometer developing under the ESA contract 4000107369-12-NL-MH (February 2013). After making several assumptions during the study (identical embedded element patterns, infinite ground plane, etc), the PAFs for C-, X- and Ku-bands have been designed and optimized in order to have a minimum number of antenna elements. The study shows

3.3. CONCLUSIONS

that all radiometer requirements can be satisfied, however, PAFs must employ many antenna elements, which is not realizable in the nearest few years due to the limitation on the power consumption when operating on a satellite. Fortunately, there are reasons to assume that this will be possible in a 5-years time frame.

Additionally, the effect of the limited dynamic range on the weight coefficients has been studied. The dynamic range is limited because there are uncertainties in the antenna system, and therefore a more precise calibration procedure is required for each receiving channel to reduce these uncertainties.

Chapter 4

Conclusions and future work

During last decades phased array feeds (PAFs) for reflector antennas have been proven to have numerous advantages over single-pixel feeds or clusters of them. However, many unsolved questions remain, among them: "What is the mechanism governing the PAF-reflector interaction and how does it affect the reflector antenna characteristics, such as its radiation pattern, directivity, receiving sensitivity, etc?" In the first part of the current work an attempt to answer this question is made. For this purpose a CBFM-PO Jacobi-iterative approach has been developed to model a large reflector antenna (with a diameter exceeding 100 wavelengths) that is fed by a complex PAF. This approach, in combination with the proposed acceleration techniques, not only allows one to solve electrically large antenna systems accurately and time-efficiently, but it also provides a physical insight in the feed-reflector mutual coupling mechanism. Several numerical computations have been performed – including for a real-world PAF system – whose conclusions are drawn at the end of Chapter 2.

The second part of the thesis is devoted to a feasibility study of PAFs in satellite radiometers for remote sensing of the sea surface. In the current work the push-broom radiometer with a toroidal reflector has been considered and the following questions have been addressed:

- to what extent can the performance of push-broom radiometers be enhanced by using dense PAFs and what are their performance-limiting factors?
- what is the minimum complexity of the PAF design (size, number of elements and their arrangement in the feed as well as the number of active receiver channels) that is required for meeting the instrument specifications at which future radiometers aim?
- what beamforming algorithms should be used to approach a certain optimality criterion on the receiving characteristics of the radiometer?

The layouts of PAFs have been optimized for a minimum number of antenna elements and a customized beamformer has been developed. It has been shown that all

radiometer requirements can be fully satisfied, and that the designed “moon”-shaped PAF allows to achieve a similar performance for all scanned beams with a minimized complexity of the feeding network with virtually identical optimal excitations. However, PAFs must employ many antenna elements, therefore, in future work, we plan to reduce their number further by improving the beamforming algorithm and reducing the focal length of the toroidal reflector. Furthermore, it should be validated how the modeling assumptions that have been made in the current studies (e.g. infinite ground plane and ignored array truncation effects) affect the radiometer performance.

Finally, it has been shown how advanced beamforming algorithms can be used to reduce the calibration complexity of the beam shape, while maintaining high receiving sensitivity for radio telescopes equipped with PAFs.

References

- [1] W. V. Cappellen, J. G. B. de Vaate, K. Warnick, B. Veidt, R. Gough, C. Jackson, and N. Roddis, “Phased array feeds for the square kilometre array,” in *General Assembly and Scientific Symposium, 2011 XXXth URSI*, Istanbul, Turkey, Aug. 2011, pp. 1–4.
- [2] J. Fisher and R. Bradley, “Full-sampling array feeds for radio telescopes,” in *Proc. SPIE, Radio Telescopes*, vol. 4015, Munich, Germany, Jul. 2000, pp. 308–318.
- [3] M. Ivashina, J. bij de Vaate, R. Braun, and J. Bregman, “Focal plane arrays for large reflector antennas: First results of a demonstrator project,” in *Proc. of the SPIE, Astronomical Telescopes and Instrumentation*, vol. 5489, Glasgow, UK, Jun. 2004, pp. 1129–1138.
- [4] D. Cavallo, A. Neto, G. Gerini, and G. Toso, “On the potentials of connected slots and dipoles in the presence of a backing reflector,” in *Proc. of 30th ESA Antenna Workshop on Antennas for Earth Observation, Science, Telecommunication and Navigation Space Missions*, Noordwijk, The Netherlands, May 2008, pp. 407–410.
- [5] D. R. DeBoer, R. G. Gough, J. D. Bunton, T. J. Cornwell, R. J. Beresford, S. Johnston, I. J. Feain, A. E. Schinckel, C. A. Jackson, M. J. Kesteven, A. Chipendale, G. A. Hampson, J. D. O’Sullivan, S. G. Hay, C. E. Jacka, T. W. Sweetnam, M. C. Storey, L. Ball, and B. J. Boyle, “Australian SKA pathfinder: A high-dynamic range wide-field of view survey telescope,” *Proc. IEEE*, vol. 97, no. 8, pp. 1507–1521, Aug. 2009.
- [6] B. Veidt, T. Burgess, R. Messing, G. Hovey, and R. Smegal, “The DRAO phased array feed demonstrator: Recent results,” in *13th Int. Symp. on Antenna Technology and Applied Electromagnetics and the Canadian Radio Science Meeting, ANTEM/URSI 2009*, Banff, Canada, Feb. 2009, pp. 1–4.
- [7] W. A. van Cappellen and L. Bakker, “APERTIF: Phased array feeds for the Westerbork synthesis radio telescope,” in *IEEE International Symposium on Proc. Phased Array Systems and Technology (ARRAY)*, Boston, Oct. 2010, pp. 640–647.

REFERENCES

- [8] M. Arts, M. Ivashina, O. Iupikov, L. Bakker, and R. van den Brink, "Design of a low-loss low-noise tapered slot phased array feed for reflector antennas," in *Proc. European Conference on Antennas and Propag. (EuCAP)*, Barcelona, Spain, Apr. 2010, pp. 1–5.
- [9] X. Bosch-Lluis, I. Ramos-Perez, A. Camps, J. F. Marchan-Hernandez, N. Rodriguez-Alvarez, E. Valencia, M. A. Guerrero, and J. M. Nieto, "Initial results of a digital radiometer with digital beamforming," in *IEEE International Geoscience and Remote Sensing Symposium, IGARSS 2008*, vol. 2, Boston, Massachusetts, U.S.A., Jul. 2008, pp. II-485–II-488.
- [10] C. Cappellin, K. Pontoppidan, P. Nielsen, N. Skou, S. S. Søbjærg, A. Ihle, D. Hartmann, M. Ivashina, O. Iupikov, and K. v. t Klooster, "Novel multi-beam radiometers for accurate ocean surveillance," in *Proc. European Conference on Antennas and Propag. (EuCAP)*, The Hague, The Netherlands, Apr. 2014, pp. 1–4.
- [11] O. A. Iupikov, M. V. Ivashina, K. Pontoppidan, P. H. Nielsen, C. Cappellin, N. Skou, S. S. Søbjærg, A. Ihle, D. Hartmann, and K. v. t Klooster, "Dense focal plane arrays for pushbroom satellite radiometers," in *Proc. European Conference on Antennas and Propag. (EuCAP)*, Hague, The Netherlands, Apr. 2014, pp. 1–5.
- [12] M. Ivashina and C. G. M. van 't Klooster, "Focal fields in reflector antennas and associated array feed synthesis for high efficiency multi-beam performances," *TIJDSCHRIFT-NERG*, vol. 68, no. 1, pp. 11–19, 2003.
- [13] W. Briskin and C. Craeye. (2004, Jan.) Focal-plane array beam-forming and spill-over cancellation using vivaldi antennas. EVLA memo 69. [Online]. Available: <http://http://www.aoc.nrao.edu/evla/geninfo/memoseries/evlamemo69.pdf>
- [14] C. Craeye, W. Briskin, and X. Dardenne, "Simulated radiation characteristics of wideband focal-plane arrays and their impact on the system gain-to-temperature ratio," in *Proc. of the JINA 2004 Conference*, Nice, France, Nov. 2004.
- [15] B. D. Jeffs, K. F. Warnick, J. Landon, J. Waldron, D. Jones, J. R. Fisher, and R. Norrod, "Signal processing for phased array feeds in radio astronomical telescopes," *IEEE J. Selected Topics in Signal Processing*, vol. 2, no. 5, pp. 635–646, Oct. 2008.
- [16] D. Hayman, T. Bird, K. Esselle, and P. Hall, "Experimental demonstration of focal plane array beamforming in a prototype radiotelescope," *IEEE Trans. Antennas Propag.*, vol. 58, no. 6, pp. 1922–1934, Jun. 2010.

REFERENCES

- [17] M. V. Ivashina, O. Iupikov, R. Maaskant, W. A. van Cappellen, and T. Oosterloo, “An optimal beamforming strategy for wide-field surveys with phased-array-fed reflector antennas,” *IEEE Trans. Antennas Propag.*, vol. 59, no. 6, pp. 1864–1875, Jun. 2011.
- [18] M. Elmer, B. Jeffs, K. F. Warnick, J. Fisher, and R. Norrod, “Beamformer design methods for radio astronomical phased array feeds,” *IEEE Trans. Antennas Propag.*, vol. 60, no. 2, pp. 930–914, Feb. 2012.
- [19] (2003, Sep.) Ska memo 40: Figure of merit for ska survey speed. [Online]. Available: https://www.skatelescope.org/uploaded/51368_40_memo_Bunton.pdf
- [20] M. V. Ivashina, M. Kehn, P.-S. Kildal, and R. Maaskant, “Decoupling efficiency of a wideband Vivaldi focal plane array feeding a reflector antenna,” *IEEE Trans. Antennas Propag.*, vol. 57, no. 2, pp. 373–382, Feb. 2009.
- [21] A. Thompson, J. Moran, and G. Swenson, *Interferometry and Synthesis in Radio Astronomy*. New York: Wiley, 2001.
- [22] J. F. Johansson, “Theoretical limits for aperture efficiency in multi-beam antenna systems,” Chalmers University of Technology (Sweden), Dept. of Radio Space Sciences, Technical Report 161, May 1988.
- [23] K. F. Warnick, M. V. Ivashina, S. J. Wijnholds, and R. Maaskant, “Polarimetry with phased array antennas: theoretical framework and definitions,” *IEEE Trans. Antennas Propag.*, vol. 60, no. 1, pp. 184–196, Jan. 2012.
- [24] S. Wijnholds, M. Ivashina, R. Maaskant, and K. F. Warnick, “Polarimetry with phased array antennas: Sensitivity and polarimetric performance using unpolarized sources for calibration,” *IEEE Trans. Antennas Propag.*, vol. 60, no. 10, pp. 4688–4698, Oct. 2012.
- [25] T. Carozzi and G. Woan, “A fundamental figure of merit for radio polarimeters,” *IEEE Trans. Antennas Propag.*, vol. 59, no. 6, pp. 2058–2065, Jun. 2011.
- [26] O. Smirnov, “Revisiting the radio interferometer measurement equation. ii. calibration and direction-dependent effects,” *Astronomy and Astrophysics*, vol. 527, Feb. 2011. [Online]. Available: <http://arxiv.org/pdf/1101.1765v3.pdf>
- [27] O. A. Iupikov, M. V. Ivashina, and O. M. Smirnov, “Reducing the complexity of the beam calibration models of phased-array radio telescopes,” in *Proc. European Conference on Antennas and Propag. (EuCAP)*, Rome, Italy, Apr. 2011, pp. 930–933.

REFERENCES

- [28] A. Young, R. Maaskant, M. V. Ivashina, and D. B. Davidson, "Performance evaluation of far field patterns for radio astronomy application through the use of the Jacobi-Bessel series," in *Proc. Int. Conf. on Electromagn. in Adv. Applicat. (ICEAA)*, Cape Town, Sep. 2012, pp. 884–887.
- [29] P. Valle, G. Orlando, R. Mizzoni, F. Heliere, and K. van 't Klooster, "P-band feedarray for biomass," in *Proc. European Conference on Antennas and Propag. (EuCAP)*, Prague, Czech Republic, Mar. 2012, pp. 3426–3430.
- [30] P. Cecchini, R. Mizzoni, G. Orlando, F. Heliere, and K. van 't Klooster, "A dual band array-fed reflector scansar antenna," in *Proc. European Conference on Antennas and Propag. (EuCAP)*, Prague, Czech Republic, Mar. 2012, pp. 3431–3435.
- [31] "Antenna requirements document," TICRA (Denmark), Technical Report S-1580-03, 2013.
- [32] (2013, Sep.). [Online]. Available: http://earthobservatory.nasa.gov/Features/EO1/eo1_2.php
- [33] P. Nielsen, K. Pontoppidan, J. Heeboell, and B. L. Stradic, "Design, manufacture and test of a pushbroom radiometer," in *Antennas and Propagation, 1989. ICAP 89., Sixth International Conference on (Conf. Publ. No.301)*, Coventry, United Kingdom, Apr. 1989, pp. 126–130.
- [34] R. Hoferer and Y. Rahmat-Samii, "RF characterization of an inflatable parabolic torus reflector antenna for space-borne applications," *IEEE Trans. Antennas Propag.*, vol. 46, no. 10, pp. 1449–1457, Oct. 1998.
- [35] S. G. Hay, J. D. O'Sullivan, J. S. Kot, C. Granet, A. Grancea, A. R. Forsyth, and D. H. Hayman, "Focal plane array development for ASKAP (australian SKA pathfinder)," in *Proc. European Conference on Antennas and Propag. (EuCAP)*, Edinburgh, UK, Nov. 2007, pp. 1–5.
- [36] K. F. Warnick, "High efficiency phased array feed antennas for large radio telescopes and small satellite communication terminals," in *Proc. European Conference on Antennas and Propag. (EuCAP)*, Gothenburg, Sweden, Apr. 2013, pp. 448–449.
- [37] A. Moldsvor and P.-S. Kildal, "Systematic approach to control feed scattering and multiple reflections in symmetrical primary-fed reflector antennas," *IEEE Trans. Antennas Propag.*, vol. 139, no. 1, pp. 65–71, Sep. 1992.
- [38] P. Bolli, G. Gentili, L. Lucci, R. Nesti, G. Pelosi, and G. Toso, "A hybrid perturbative technique to characterize the coupling between a corrugated horn and a

REFERENCES

- reflector dish," *IEEE Trans. Antennas Propag.*, vol. 54, no. 2, pp. 595–603, Sep. 2006.
- [39] M. Bandinelli, F. Milani, G. Guida, M. Bercigli, P. Frandsen, S. Sorensen, B. Bencivenga, and M. Sabbadini, "Feed-array design in presence of strong scattering from reflectors," in *Proc. European Conference on Antennas and Propag. (EuCAP)*, Rome, Italy, Apr. 2011, pp. 3844–3848.
- [40] C. D. Giovampaola, E. Martini, A. Toccafondi, and S. Maci, "A hybrid PO/generalized-scattering-matrix approach for estimating the reflector induced mismatch," *IEEE Trans. Antennas Propag.*, vol. 60, no. 9, pp. 4316–4325, Sep. 2012.
- [41] W. A. van Cappellen and L. Bakker. (2010) Eliminating sensitivity ripples in prime focus reflectors with low-scattering phased array feeds. [Online]. Available: http://csas.ee.byu.edu/docs/Workshop/BYU_StandingWaves_Cappellen.pdf
- [42] R. E. Hodges and Y. Rahmat-Samii, "An iterative current-based hybrid method for complex structures," *IEEE Trans. Antennas Propag.*, vol. 45, no. 2, pp. 265–276, Feb. 1997.
- [43] C. S. Kim and Y. Rahmat-Samii, "Low profile antenna study using the physical optics hybrid method (POHM)," in *Proc. IEEE AP-S International Symposium*, Ontario, Canada, Jun. 1991, pp. 1350–1353.
- [44] J. M. Taboada and F. Obelleiro, "Including multibounce effects in the moment-method physical-optics (MMPO) method," *Micr. Opt. Technol.*, vol. 32, no. 6, pp. 435–439, 2002.
- [45] U. Jakobus and F. M. Landstorfer, "Improved PO-MM hybrid formulation for scattering from three-dimensional perfectly conducting bodies of arbitrary shape," *IEEE Trans. Antennas Propag.*, vol. 43, no. 2, pp. 162–169, Feb. 1995.
- [46] B. Andrés-García, D. Gonzalez-Ovejero, C. Craeye, L. García-Muñoz, and D. Segovia-Vargas, "An iterative MoM-PO method based on a MBF/Krylov approach," in *Proc. European Conference on Antennas and Propag. (EuCAP)*, Barcelona, Spain, Apr. 2010, pp. 1–4.
- [47] S. Hay, R. Mittra, and N. Huang. (2010) Analysis of reflector and feed scattering and coupling effects on the sensitivity of phased array feeds. [Online]. Available: <http://csas.ee.byu.edu/docs/Workshop/BYUSGH.pdf>
- [48] G. Harp, R. F. Ackermann, Z. J. Nadler, S. Blair, M. Davis, M. C. H. Wright, J. R. Forster, D. DeBoer, W. J. Welch, S. Atkinson, D. Backer, P. R. Backus,

REFERENCES

- W. Barott, A. Bauermeister, L. Blitz, D. C. J. Bock, G. Bower, T. Bradford, C. Cheng, S. Croft, M. Dexter, J. Dreher, G. Engargiola, E. D. Fields, C. Heiles, T. Helfer, J. Jordan, S. Jorgensen, T. Kilsdonk, C. Gutierrez-Kraybill, G. Keating, C. Law, J. Lugten, D. H. E. MacMahon, P. McMahon, O. Milgrome, A. Siemion, K. Smolek, D. Thornton, T. Pierson, K. Randall, J. Ross, S. Shostak, J. Tarter, L. Urry, D. Werthimer, P. Williams, and D. Whyson, "Primary beam and dish surface characterization at the Allen telescope array by radio holography," *IEEE Trans. Antennas Propag.*, vol. 59, no. 6, pp. 2004–2021, Jun. 2011.
- [49] W. Van Cappellen and M. Ivashina, "Temporal beam pattern stability of a radio astronomy phased array feed," in *Proc. European Conference on Antennas and Propag. (EuCAP)*, Rome, Italy, Apr. 2011, pp. 926–929.
- [50] O. A. Iupikov, R. Maaskant, M. Ivashina, A. Young, and P. Kildal, "Fast and accurate analysis of reflector antennas with phased array feeds including multiple reflections between feed and reflector," *IEEE Trans. Antennas Propag.*, vol. 62, no. 7, Jul. 2014.
- [51] P.-S. Kildal, "Factorization of the feed efficiency of paraboloids and cassegrain antennas," *IEEE Trans. Antennas Propag.*, vol. 33, no. 8, pp. 903–908, Aug. 1985.
- [52] N. M. Kehn, M. V. Ivashina, P.-S. Kildal, and R. Maaskant, "Definition of unifying decoupling efficiency of different array antennas – case study of dense focal plane array feed for parabolic reflector," *Int. Journal of Electronics and Communications (AEU)*, vol. 64, no. 5, pp. 403–412, May 2010.
- [53] P.-S. Kildal, S. Skyttemyr, and A. Kishk, "G/T maximization of a paraboloidal reflector fed by a dipole-disk antenna with ring by using the multiple-reflection approach and the moment method," *IEEE Trans. Antennas Propag.*, vol. 45, no. 7, pp. 1130–1139, Jul. 1997.
- [54] S. N. Makarov, *Antenna and EM Modeling With MATLAB*. New York: John Wiley and Sons, Inc., 2002.
- [55] R. Maaskant, "Analysis of large antenna systems," Ph.D. dissertation, Electrical engineering, Eindhoven University of Technology, Eindhoven, 2010. [Online]. Available: <http://alexandria.tue.nl/extra2/201010409.pdf>
- [56] R. Maaskant, M. V. Ivashina, O. Iupikov, E. A. Redkina, S. Kasturi, and D. H. Schaubert, "Analysis of large microstrip-fed tapered slot antenna arrays by combining electrodynamic and quasi-static field models," *IEEE Trans. Antennas Propag.*, vol. 56, no. 6, pp. 1798–1807, Jun. 2011.

REFERENCES

- [57] (2007) EM Software & Systems – S.A. (Pty) Ltd, Stellenbosch, South Africa, FEKO, Suite 6.0. [Online]. Available: <http://www.feko.info>
- [58] B. A. Munk, *Finite Antenna Arrays and FSS*. Danvers, Massachusetts: John Wiley & Sons, Inc., 2003.
- [59] J. J. H. Wang, “An examination of the theory and practices of planar near-field measurement,” *IEEE Trans. Antennas Propag.*, vol. 36, no. 6, pp. 746–753, Jun. 1988.
- [60] J. P. McKay and Y. Rahmat-Samii, “Compact range reflector analysis using the plane wave spectrum approach with an adjustable sampling rate,” *IEEE Trans. Antennas Propag.*, vol. 39, no. 6, pp. 746–753, Jun. 1991.
- [61] R. C. Rudduck, D. C. Wu, and M. Intihar, “Near-field analysis by the plane-wave spectrum approach,” *IEEE Trans. Antennas Propag.*, vol. 21, no. 2, pp. 231–234, Mar. 1973.
- [62] C. A. Balanis, *Advanced Engineering Electromagnetics*. New York: John Wiley and Sons, Inc., 1989.
- [63] M. V. Ivashina, R. Maaskant, and B. Woestenburger, “Equivalent system representation to model the beam sensitivity of receiving antenna arrays,” *IEEE Antennas Wireless Propag. Lett.*, vol. 7, no. 1, pp. 733–737, Jan. 2008.
- [64] “Technical note 1,” TICRA (Denmark), DTU-Space (Denmark), Technical Report S-1580-02, 2013.
- [65] M. Ivashina, M. Kehn, and P.-S. Kildal, “Optimal number of elements and element spacing of wide-band focal plane arrays for a new generation radio telescope,” in *IEEE Trans. Antennas Propag.*, Edinburgh, UK, Nov. 2007, pp. 1–7.
- [66] H. L. van Trees, *Optimum Array Processing – Part IV of Detection, Estimation, and Modulation Theory*. New York: Wiley, 2002.
- [67] N. Skou, personal communication, 2014.
- [68] “Technical note 5,” TICRA (Denmark), DTU-Space (Denmark), Chalmers (Sweden), HPS (Germany), Technical Report S-1580-TN5, 2014.
- [69] S. Ellingson, T. Clarke, A. Cohen, J. Craig, N. Kassim, Y. Pihlstrom, L. Rickard, and G. Taylor, “The long wavelength array,” *IEEE Trans. Antennas Propag.*, vol. 97, no. 8, pp. 1421–1430, Aug. 2009.
- [70] M. D. Vos, A. Gunst, and R. Nijboer, “The lofar telescope: System architecture and signal processing,” *IEEE Trans. Antennas Propag.*, vol. 97, no. 8, pp. 1431–1437, Aug. 2009.

REFERENCES

- [71] The SKA website. [Online]. Available: <http://www.skatelescope.org/>
- [72] V. Galindo-Israel and R. Mittra, "A new series representation for the radiation integral with application to reflector antennas," *IEEE Trans. Antennas Propag.*, vol. 55, no. 5, pp. 631–641, Sep. 1977.
- [73] Y. Rahmat-Samii and V. Galindo-Israel, "Shaped reflector antenna analysis using the Jacobi-Bessel series," *IEEE Trans. Antennas Propag.*, vol. 28, no. 4, pp. 425–435, Jul. 1980.
- [74] O. I. Frost, "An algorithm for linearly constrained adaptive array processing," *Proceedings of the IEEE*, vol. 60, no. 8, pp. 926–935, Aug. 1972.
- [75] I. Theron, R. Lehmensiek, and D. de Villiers, "The design of the meerkat dish optics," in *Proc. Int. Conf. on Electromagn. in Adv. Applicat. (ICEAA)*, Cape Town, Sep. 2012, pp. 539–542.